# Transition to magma-driven rifting in the South Turkana Basin: Part 2

Tyrone O. Rooney[1*], Paul J. Wallace[2], James D. Muirhead[3,4], Brandon Chiasera[1], R. Alex Steiner[1], Guillaume Girard[1,5], Jeffery A. Karson[3]

*[1]Dept. of Earth and Environmental Sciences, Michigan State University, East Lansing, MI 48823, USA*
*[2]Department of Earth Sciences, University of Oregon, Eugene, Oregon 97403-1272, USA*
*[3]Department of Earth Sciences, Syracuse University, Syracuse, New York 13244, USA*
*[4]School of Environment, University of Auckland, Auckland 1142, New Zealand*
*[5]Department of Earth, Atmosphere, and Environment, Northern Illinois University, DeKalb, IL 60115, USA*

*Corresponding author: rooneyt@msu.edu

**Abstract:**

Strain localization is central to the transition between continental rifting and seafloor spreading. In the East African Rift System (EARS) there is an emerging understanding of the link between extensional pulses and magmatic episodes. We investigate modern magmatism located within the Turkana Depression and its relationship to the distribution of extensional strain. We probe the source of magmatism at South Island volcano using bulk rock, melt inclusion, and olivine geochemical data and find that the magmas are derived from sub-lithospheric sources equivalent to magmatism in the more mature sectors of the rift. The depth extent of the magmatic plumbing system of South Island is constrained using vapor saturation pressures derived from bubble-corrected $H_2O$ and $CO_2$ concentrations in melt inclusions, and results indicate a magmatic system resembling modern axial volcanic systems observed in other parts of the EARS. The zone of focused axial magmatism that South Island represents has evolved contemporaneously with a region of focused axial faulting that has accommodated the majority of regional Holocene extension and subsidence at this latitude. We conclude that at South Island there has been a migration of magmatic and tectonic strain towards the modern zone of focused intrusion along this portion of the EARS.

**Supplementary material:** S1-S2 image files, data table files S3-S6, and caption file S7 are available at http://geolsoc.figshare.com.

The localization of strain within a continental rift environment is central to the transition between continental rifting and sea-floor spreading (e.g., Naliboff et al., 2017). Tectonic extension, which may initially result in more diffuse thinning of the brittle continental lithosphere (e.g., Autin et al., 2010), become progressively more concentrated within rift valleys as they evolve towards an oceanic rift (e.g., Illsley-Kemp et al., 2018). Magmatism and associated lithospheric weakening (e.g., Buck, 2006; Bialas et al., 2010) play an important role localizing extensional strain during rift development (Behn et al., 2006; Beutel et al., 2010; Muirhead et al., 2016) and controlling the transition from thinning continental lithosphere to the formation of new oceanic lithosphere (e.g., Bastow and Keir, 2011). However, key unknowns in this transitional process are the timing, distribution, and volume of magmatism in relation to extension (e.g., Peron-Pinvidic et al., 2019).

The East African Rift System (EARS) represents the premier example of modern continental rifting, displaying a range of rift conditions from relatively magma-poor basins in southern rift sectors (e.g., Lake Malawi Rift), to magma-rich basins (e.g., Main Ethiopian Rift) farther north (e.g., Ebinger, 1989; Chorowicz, 2005; Macgregor, 2015; Morley and Ngenoh, 1999; Purcell, 2018). In the Eastern Branch of the East African Rift System (Fig. 1) there is an emerging understanding of the link between extensional pulses and associated magmatic episodes over both short (e.g., Wright et al., 2006; Ayele et al., 2009; Ebinger et al., 2010; Belachew et al., 2012) and longer timescales (Macgregor, 2015; Purcell, 2018; Rooney, 2020b, 2020a). Modern magmatic activity in the Eastern Branch manifests within the rift as axial zones of focused magmatic-tectonic activity (Ebinger and Casey, 2001; Keranen et al., 2004; Keir et al., 2006), extending from Afar in the north to southern regions of the Kenya Rift (Weinstein et al., 2017). Throughout much of its length, the Eastern Branch is characterized by narrow rift valleys where the migration of strain from rift border faults to zones of focused magmatism and tectonism is well-characterized (e.g., Boccaletti et al., 1998; Ebinger and Casey, 2001; Wolfenden et al., 2004; Casey et al., 2006; Rooney et al., 2011; Muirhead et al., 2016). However, where the Eastern Branch intersects pre-thinned lithosphere, either resulting from earlier phases of Mesozoic to Paleogene rifting in Turkana or Miocene rifting in Afar (e.g., Red Sea Rift), wider depressions can form that exhibit more complex rift basin geometries and segmentation styles (e.g., Dunkelman et al., 1988; Hendrie et al., 1994; Morley et al., 1999; Manighetti et al., 2001; Tesfaye et al., 2003; Le Gall et al., 2005, 2010; Vétel et al., 2005; Koptev et al., 2018). Locating the current loci of magmatic and tectonic strain accommodation can be challenging in these broad depressions (e.g., Brune et al., 2017; Corti et al., 2019; Knappe et al., 2020; Wang et al., 2021).

Here, we investigate the nature of modern magmatism within the broadly rifted Turkana Depression in East Africa, and its relationship to the evolving distribution of extensional strain. We present a geochemical and volatile element study of South Island, the most mature volcanic edifice within the modern axial center traversing Lake Turkana (Bloomer et al., 1989; Karson and Curtis, 1994; Furman et al., 2004). We probe the source of magmatism using major and trace element data derived from both whole-rocks and melt inclusions and provide laser-ablation ICPMS analysis of olivine phenocrysts. We constrain the depth extent of the magmatic plumbing system of South Island using vapor saturation pressures derived from bubble-corrected $H_2O$ and $CO_2$ concentrations in olivine-hosted melt inclusions. We find that magmas from South Island exhibit sub-lithospheric sources that closely resemble the modern axial volcanic systems observed in the Eastern Branch (e.g. Quaternary volcanic segments of the Main Ethiopian Rift) (Rooney, 2020d). Furthermore, we find that the magmatic plumbing system situated below South Island is located in the mid-crust and has evolved contemporaneously with a region of focused axial faulting that has accommodated the majority of Quaternary – Recent regional extension (Muirhead et al., this volume). We conclude that at South Island there has been a migration of magmatic and tectonic strain towards the modern zone of focused intrusion along this portion of the East African Rift System in Turkana.

## 2. Background

### 2.1 East African Rift System

South Island is located within the South Turkana basin of Lake Turkana, an important geographic feature of the Turkana Depression (Fig. 1;2). The Turkana Depression is a region of diffuse extension within the Cenozoic EARS, lying between the significantly narrower Kenya Rift to the south, and Main Ethiopian Rift to the north (e.g., Ebinger and Ibrahim, 1994; Mechie et al., 1997; Keranen et al., 2004; Mackenzie et al., 2005; Mariita and Keller, 2007). The low elevation of the Turkana Depression is in contrast to the uplifted domes evident to the north and south and may relate to the extended interval over which lithospheric extension has been operating in this region and the isostatic response of the thin crust (e.g., Benoit et al., 2006; Boone et al., 2019). Beginning in the early Cretaceous, the area of the future Turkana Depression became part of the Anza rift, which linked other Mesozoic rift basins in Kenya and Sudan (Bosworth, 1992; Bosworth and Morley, 1994). These Mesozoic rifting events presumably thinned the continental lithosphere prior to the initiation of the EARS. It is therefore unsurprising that the Turkana Depression marks some of the earliest manifestations of rifting within the EARS and acted as a nexus for various pulses of extensional activity and associated magmatism throughout the Cenozoic (Macgregor, 2015; Purcell, 2018; Boone et al., 2019). These protracted phases of rifting have significantly attenuated the crust (20 km) compared to other parts of the Kenya Rift (35 km) (Mechie et al., 1997; Prodehl et al., 1997; Benoit et al., 2006), with the crustal thickness of the Turkana Depression resembling the highly extended crust of the modern Afar Depression (Maguire et al., 2006).

## 2.2 Cenozoic Magmatism of the East African Rift System

Cenozoic magmatism in East Africa is thought to be related to the overlapping effects of lithospheric extension and the upwelling of thermo-chemically anomalous material from the African Large Low Shear Velocity Province (Rooney, 2020d). The earliest manifestations of East African Cenozoic magmatism (Initial Eocene Phase: Rooney, 2017) were centered on Southern Ethiopian basins and the Turkana Depression from ca. 45-34 Ma (e.g., Ebinger et al., 1993, 2000; George et al., 1998; Furman et al., 2006b; Rooney, 2017), and were volumetrically dominated by flood basalts with intervals of more evolved compositions (Davidson, 1983; Steiner et al., 2021). The subsequent Oligocene Traps phase (33.9-27 Ma: Rooney, 2017) resulted in the expansion of volcanism throughout East Africa and Yemen and the notable formation of the flood basalts of the NW Ethiopian plateau (e.g., Mohr and Zanettin, 1988; Baker et al., 1996; Krans et al., 2018; Pik et al., 1999; Rooney et al., 2018). The Early Miocene Resurgence phase (ca. 28 Ma – 20 Ma: Rooney, 2017, 2020b) manifests as another geographically widespread (though volumetrically smaller) pulse of dominantly basaltic volcanism occurring throughout East Africa. There then followed two more pulses of basaltic volcanism at ca. 12-9 Ma (Mid-Miocene Resurgence Phase) and ca. 4 Ma (Stratoid Phase), which are considered to have originated in Turkana and Afar (Rooney, 2020b). Modern volcanic activity in the Eastern Branch of the EARS dominantly occurs within axial or rift marginal graben and is dominated by large silicic volcanoes and small cinder cones and associated flows.

## 2.3 Quaternary magmatism in Turkana

Quaternary magmatic activity in Turkana broadly bifurcates into magmatism associated with the Mega/Megado area and Dilo-Dukana area in the Ririba Rift (Conticelli et al., 1999; Orlando et al., 2006; Shinjo et al., 2011; Corti et al., 2019; Franceschini et al., 2020) and the axial volcanic islands of Lake Turkana in the Kenyan Rift (the focus of this study) (Fig. 2). Pliocene to Quaternary activity also occurs on the Huri Hill shield (Class et al., 1994). The main axial volcanic centers of the Kenyan rift in Turkana and adjacent areas are (from north to south) the Korath Range in southern Ethiopia (Brown and Carmichael, 1969; Jicha and Brown, 2014), North Island (Brown and Carmichael, 1971; Karson and Curtis, 1994; Furman et al., 2006b), Central Island (including Birds Nest) (Dunkelman et al., 1988; Karson and Curtis, 1994; Furman et al., 2006b), South Island (Brown and Carmichael, 1971; Karson and Curtis, 1994; Furman et al., 2006b), and the Barrier, Namarunu, and Emuruangogolak in the very south (Ochieng et al., 1988; Dunkley et al., 1993) (Fig. 2). These main volcanic centers are located within several half graben segments that are kinematically linked along the rift (Karson and Curtis, 1994) and produced a wide range of magma compositions that are dominantly basalts and trachytes with subordinate silicic pyroclastics and rhyolites (Ochieng et al., 1988; Dunkley et al., 1993). Since the mid-Pliocene, faulting and subsidence in Turkana has primarily focused within the lake-basin segments that now host three main volcanic islands in Lake Turkana (Karson and Curtis, 1994; Morley et al., 1999). These basins are linked by accommodation fault zones and have accumulated significant volumes of Plio-Pleistocene sediments (e.g., 1-2 km of sediments in South Turkana basin). The Islands of Turkana are spaced approximately 43±5 km apart (Mohr and Wood, 1976) and each lies within the center of a graben or half graben (Dunkelman et al., 1988). Similarities between the islands exist in terms of structure, stratigraphy, and lithologic history, with minor variation evident in terms of composition and mineralogy. South Island is the most mafic and heavily faulted member of the three islands, and has the greatest subaerial volume (4 $km^3$) and total volume above the lake floor (14 $km^3$), which is several times that of the other Turkana volcanic islands (Karson and Curtis, 1994). Axial faults associated with these volcanic islands run parallel to the rift, and the morphologies of smaller volcanic cones support rift parallel axial diking below the South Island (See Figure 2 of Muirhead et al., this volume), with these dike intrusions possibly extending into lakebed sediments (Karson and Curtis, 1994; Muirhead et al., this volume).

**2.4 South Island**

The absolute age range of products of the South Island volcano is unclear; however, it has been hypothesized to be Quaternary, with much of the activity post-dating 3.2 ka (Dunkley et al., 1993). Karson & Curtis (1994) observed South Island flows on the eastern side of the island are the freshest in the region, with the exception of the historic 1888 eruption of Teleki's Cone of the Barrier. Fumarolic activity from one of the South Island craters was observed in 1888 by Teleki's expedition (von Höhnel, 1894), consistent with the young age of the lavas and active solfataras (Fig. S1). The most pronounced feature of the island are the cinder cones that are associated with a series of vents running north to south across the length of the Island.

Following the stratigraphic nomenclature of Karson & Curtis (1994), the earliest eruptions of the South Island volcano were basaltic flows of unit S1 (Fig. 3), followed by two eruptions producing tuff units S2 and S3, which are separated by an unconformity. Recent seismic stratigraphic investigations of the South Turkana basin (Morrissey and Scholz, 2014) reveal that this unconformity is likely associated with uplift and relative lake level drop, which is also evident in terraces at the north end of the island (Garcin et al., 2012; Melnick et al., 2012). The next volcanic eruption produced a second unit, S4, of basaltic flows. South Island's surface is dotted with spatter cones associated with lavas of unit S4, which can reach up to 400 m high and are made of scoria, agglutinate, lava flows, and have rare basaltic dikes cross cutting them (Karson and Curtis, 1994). The most recent deposit is an unconsolidated ashfall unit, S5.

**2.5 Sources of Quaternary magmatism in Turkana**

There exists a spatial heterogeneity in the composition of basaltic lavas occurring along the length of this rift sector that was initially identified by Furman et al. (2004) in terms of an amphibole-bearing lithospheric mantle source for many lavas at Bird's Nest and Central Island, and a fertile peridotite for other lavas (including South Island). Furman et al. (2004) notes that the isotopic composition of lavas from these islands is also consistent with a strong contribution from the Afar Plume, in particular in lavas from South Island where hydrous mantle phases were not likely present in the source of these lavas (based on trace element patterns) and the source is interpreted as a plume-influenced upper mantle. There is no existing interpretation as to the specific source of lavas from Korath, though Bloomer et al. (1989) using the limited data from Brown & Carmichael (1969) hypothesized a veined mantle source for Korath, and for all the Quaternary Islands of Lake Turkana.

## 3. Methods

### 3.1 Samples

During a field expedition undertaken by Jeffrey Karson and Patchin Curtis to South Island in 1992, 18 samples (SI92-1 through SI92-18) that represented the diversity of lithologies present on the island were collected. Lithologies identified on South Island include two flow units S1 and S4, two tuff units S2 and S3, and a top layer of unconsolidated ash, S5 (Fig. 3). Unit names follow a stratigraphic arrangement as represented in Figure 3 with S1 at the base, to S5 at top. Samples examined in this study are from S4 and are typically phenocryst-rich scoria with up to 55% volume phenocrysts (e.g., SI92-12). The dominant mineral assemblage in most samples is plagioclase + augite + olivine, however, plagioclase in most samples exhibits a degree of instability, demonstrated by anhedral phenocrysts exhibiting sieve texture. In samples SI92-12 and SI92-16 olivine phenocrysts can range up to 1 cm in size. Samples showed no obvious weathering or other secondary alteration. We have undertaken bulk rock analyses on scoria samples SI92-12 through SI92-18, collected from what we interpret as the spatter cones related to unit S4 (precise location information is unavailable). In addition, we selected a sample (SI92-16) for the analysis of melt inclusions.

### 3.2 Bulk sample processing and analytical techniques

Bulk rock analyses of samples SI92-12 through SI92-18 were undertaken at Michigan State University. Whole rock samples were cut, polished, washed in deionized water and the resulting billets were powdered in a BICO disk mill fitted with ceramic contamination control grinding plates. Sample powders were fused into homogenous glass disks using a lithium tetraborate fluxing agent. These disks were then analyzed for major elements by X-ray fluorescence (XRF) with a Bruker S4 PIONEER X-ray fluorescence spectrometer, using methods described elsewhere (Rooney et al., 2012b). The same sample disks were then analyzed in triplicate for trace elements using laser-ablation inductively coupled plasma mass spectrometer (LA-ICPMS) with a Photon-Machines Analyte G2 excimer laser and Thermo Scientific ICAP Q quadrupole ICP-MS using methods described elsewhere (Rooney et al., 2015). The XRF and LA-ICPMS sample analyses, in addition to quality assurance information, are presented in the supplementary data files S3 and S4.

### 3.3 Melt inclusion analysis – volatile elements

Olivine was separated from whole rock sample SI92-16 by crushing and handpicking. Olivine and one augite crystal (melt inclusion MSU – 01) containing melt inclusions were then selected for further processing. Melt inclusions were doubly intersected by grinding of the crystal host at the University of Oregon, and photographs were taken of whole crystals and their polished crystal wafers (Fig. S2). Nine melt inclusion samples from eight discrete crystals were prepared:

MSU – 01, 02, 03, 04, 05, 06, 07a, 07b, 08. The melt inclusions were glassy, with no daughter crystals. All melt inclusions contained vapor bubbles.

Melt inclusions were analyzed on a Thermo-Nicolet Nexus 670 Fourier-transform infrared (FT-IR) spectrometer interfaced with a Continuum IR microscope at the University of Oregon. $H_2O$ concentrations were calculated from IR peak absorbance values using the Beer-Lambert Law. $H_2O$ concentration was determined using the 3570 $cm^{-1}$ $OH^-$ peak, with molar absorption coefficient $\varepsilon = 63$ from Dixon et al. (1995). The molar absorption coefficient for $CO_2$ as carbonate is compositionally dependent. We used the major element composition of each melt inclusion to calculate the appropriate value based on Dixon and Pan (1995). The absorbance of $CO_2$ as carbonate was measured using a peak-fitting program that uses a background subtraction of carbonate-free basaltic glass (S. Newman, unpublished). Thickness was determined using the interference fringe method (e.g. Wysoczanski and Tani, 2006). Hydrous glass densities were determined by iteration between calculated glass densities (Luhr, 2001) and Beer-Lambert calculations.

The effect of post-entrapment bubble formation on the original volatile content of trapped melt inclusions was corrected using the MIMiC software (Rasmussen et al., 2020). Input parameters are listed in the supplement (Table S6) and assume a 5°C/sec cooling rate. Both bubble-corrected (solid color) and uncorrected values (partially transparent) are shown in subsequent plots.

### 3.4 Olivine and Melt inclusion compositional analysis – major and trace elements

Following FTIR measurement of $CO_2$ and $H_2O$ (where applicable as noted above), melt inclusions and host olivine crystals (and a single augite) were analyzed for major and trace elements using LA-ICPMS (Table S5). Crystals and melt inclusions analyzed were MSU-01, 02, 04, 05, 06, 07a, 07b, 08. Analysis of melt inclusion MSU-08 was not successful, and for processing of the volatile data an average of the other glass compositions was used. The analyses, conducted at Michigan State University, used the same equipment and standards as the bulk rock data methods described above, but implemented a slightly modified method wherein multiple spots per inclusion were characterized. Laser spot size was set at 30 μm. . Laser fluence was 4.11 J/cm$^2$; the instrument was placed in energy stability mode with energy set point of 3.5 mJ with a repetition rate of 10 Hz. Major and trace element data were calibrated and processed using the Thermo-Fisher data reduction software – QTegra, and normalized to an internal standard of 100% sum of the major element oxides. Spot analysis averaged about four per melt inclusion and seven per olivine. Bubbles and rims of melt inclusions were avoided during analysis. Drift was monitored by the repeated analysis of fused powder standards JB-2 and natural basalt glass standard BHVO-2G, data were corrected for drift. The NMNH Standard 111312-77 'San Carlos' olivine was also analyzed as an unknown to monitor matrix effects. Major and trace element data for individual spot analyses of melt inclusions and olivine are presented in the supplemental data tables. The average value per olivine crystal is illustrated in the accompanying figures. The average value for each melt inclusion was corrected for post-entrapment crystallization (PEC) using MIMiC (Rasmussen et al., 2020; see details below), and the corrected major element values are shown in the figures. Because the melt inclusions were all close to equilibrium with their host olivine (maximum PEC = 2.5% olivine), the corrected values are very close to the analyzed values. No major element PEC correction was made to the clinopyroxene-hosted melt inclusion (MSU-01). A bubble correction for $CO_2$ in this inclusion was made by using the median value for percent $CO_2$ lost to bubble (from MIMiC) in the other seven olivine-hosted inclusions.

## 4. Results

### 4.1 Bulk rock major and trace element geochemistry

Assuming $Fe^{3+}$ /∑Fe of 0.15, the samples being nominally volatile free, and using the methods of Le Maitre (2002), all bulk rock samples classify as nepheline-normative (2.3 to 4.6% Ne) alkali basalts, with the exception of the more evolved sample in the dataset SI92-17 (mugearite). Our new major and trace element data plot in the same fields as previous studies from South Island (Brown and Carmichael, 1971; Furman et al., 2004) (Fig. 4). When considered collectively, whole rock compositional data from the Quaternary volcanoes of Lake Turkana (Barrier, South Island, Birds Nest, Central Island, North Island) form coherent arrays versus an index of differentiation (i.e., MgO), which suggest similarities in magmatic process occurring throughout this region, despite being discrete systems.

Chondrite-normalized REE patterns (Boynton, 1984) exhibit parallel behavior and overlap the existing datasets (Fig. 5). Primitive mantle normalized patterns (Sun and McDonough, 1989) reflect the similarities in the chondrite-normalized figures and show broadly the same pattern that is dominated by a profound peak in Nb and Ta concentrations (Fig. 6). While the use of tungsten carbide as a grinding medium in older datasets might have resulted in anomalously high Ta values, our newly collected whole rock data (ground in a ceramic disk mill) and melt inclusion data confirms the magmatic nature of this Nb-Ta anomaly. The single more evolved sample (SI92-17; MgO ~ 2 wt. %), deviates from the coherent patterns evident in the more primitive samples and has notable negative anomalies in Ti and Sr (Fig. 6).

South Island lavas share some of the same characteristics of primitive mantle normalized patterns of other lavas in the Lake Turkana region (Fig. 6). For example, all samples from the region are dominated by a profound peak in Nb and Ta concentrations (Fig. 6). However, there also exist some important differences: lavas from South Island lack the prominent negative Zr-Hf trough evident in many Barrier samples and one Birds Nest sample (Fig. 6), which suggests some differences in the source of magmas in the region. The distinctive primitive mantle normalized trace element pattern observed in South Island is also common in basaltic magmas found throughout the East African Rift System (Rooney, 2020d), the implications of which are presented in the discussion.

### 4.2 Olivine geochemistry

The olivine hosts for melt inclusions have core compositions ranging from ~$Fo_{74}$ to $Fo_{80}$ (Supplemental Table; Fig. 7). Ni, Ca, Mn exhibit similar patterns to other regional datasets, though Cr is notably depleted (Fig. 7), and may be suggestive of significant pyroxene co-fractionation. We show the South Island olivine dataset relative to high-precision olivine datasets derived from melting of different source lithologies (Sobolev et al., 2007; Foley et al., 2011; Rooney et al., 2017), however the relatively evolved composition of the olivine in South Island likely renders the control on olivine composition from source as secondary to magma evolution processes. Of note, however, is the dissimilarity of South Island olivine to those from Gerba Guracha, a Miocene alkaline volcanic center in Ethiopia where there are resolvable differences in olivine chemistry between sub-lithosphere derived melts (alkaline basalts), lithosphere-derived melts (pyroxene melanephelinites), and mixtures of the two (basanites) (Rooney et al., 2017) (Fig. 7). Accordingly, while the olivine from South Island lavas overlap other olivine from alkaline/subalkaline lavas from East Africa, they notably do not plot in the same fields as olivine from the lithospherically-derived Gerba Guracha lavas.

### 4.3 Melt inclusions

#### 4.3.1 Major and trace element data

The mean value of multiple analyses of each melt inclusion was corrected for potential post entrapment crystallization and Mg-Fe diffusive reequilibration using MIMiC (Rasmussen et al., 2020). Host olivines have Fo values that range from 74 to 80. Based on a comparison with whole rock data, we assumed an FeO* value of 10.5 wt% for the melt inclusions at the time of trapping, and we used the $K_D$ model of Toplis (2005) at the QFM buffer. All melt inclusion compositions were close to equilibrium with their olivine hosts. Because the PEC correction was less than 2.5%, no mass corrections were applied to the trace element data.

Major and trace element data show South Island melt inclusions plot in the same fields as the whole rock samples from South Island (Fig. 4), though they occupy a much more restricted range of compositions (~4-6 wt.% MgO), compared with the whole rock data (~2-12 wt.% MgO), likely due to the limited sample set. Chondrite-normalized REE values of the melt inclusions are similar to the whole-rock data (Fig. 5) but exhibit a more limited range in fractionation of La/Yb, which occurs at the low end of the whole rock data range (Fig. 4). Primitive mantle normalized patterns are largely the same as the whole rock data (Fig. 6). One exception to this is well-characterized (n = 5 spots analyzed) inclusion MI-7a, which exhibits the most extreme depletion in the most incompatible trace elements pattern in any rock from the Lake Turkana area (Fig. 6) yet exhibits concentrations of MgO and compatible elements (Ni, Cr) that are in the same range as the other melt inclusions (Supplemental Information). These data suggest that the melt inclusions trapped by the olivine mostly reflect the same melts that have constructed South Island.

#### 4.3.2 Water and carbon dioxide content of South Island melt inclusions

South Island melt inclusions yield a tightly constrained $H_2O$ content of 0.93 to 1.06 wt % $H_2O$ (Fig. 8). These $H_2O$ contents are consistent with other melt inclusions in the East African Rift System at similar values of MgO, with the exception of melt inclusions from Erta 'Ale and some samples from Nyamuragira, which have lower $H_2O$ as a result of diffusive loss during experimental rehomogenization, natural slow cooling, and/or degassing before entrapment (e.g., Head et al., 2011; Field et al., 2012).

Measured $CO_2$ concentrations in the South Island melt inclusions ranged from ~1140-2240 ppm. The volatile results from South Island are the first in East Africa to include correction for the effects of post-entrapment bubble formation on the $CO_2$ contents of the melt inclusions. This correction resulted in $CO_2$ that was between ~250 and 760 ppm higher (median ~420 ppm) in corrected melt inclusions in comparison to the measured values. After correction, the $CO_2$ concentrations in the South Island melt inclusions ranged from 1386 to 2891 ppm (Fig. 8). Considering melt inclusions from other axial magmas (<55 wt % $SiO_2$) in the Eastern Branch of the EARS, South Island $CO_2$ values overlap those of the well-developed Kone sector of the Main Ethiopian Rift (Wonji Fault Belt: Mohr, 1967; Ebinger and Casey, 2001; Rooney et al., 2007; Furman et al., 2006a) (Fig. 8).

## 5. Discussion

### 5.1 Source of Magmatism

Common patterns of occurrence of different magma types in space or time throughout East Africa has resulted in the clustering of magmas into six distinct types based upon their primitive mantle normalized patterns (Rooney, 2020d). (Rooney, 2020c). These patterns reveal insights into the source heterogeneity of East African lavas and are therefore useful indicators as to the source of the melts in this region. Three of six standard magma types have been identified in Quaternary Turkana lavas: Type II magma, typified by a broad enrichment in incompatible trace elements and a distinct negative K anomaly. These melts likely originate from the destabilization of enriched metasomes derived from the lithospheric mantle. Type III magma, typified by positive Ba and Nb-Ta anomalies and a negative U-Th anomaly. These melts are interpreted as being derived from a sub-lithospheric source (i.e., plume influenced upper mantle). Type IV magmas, typified by a hybrid of the Type II and III patterns, are thought to reflect melts of an enriched lithospheric mantle metasome mixing with melt derived from sub-lithospheric reservoirs.

The whole rock and melt inclusion data all show the same trace element patterns at South Island – evidence of a strong Type III magma signature that is indicative of predominant contributions from a hybrid sub-lithospheric source (Fig. 6), equivalent to the plume-influenced upper mantle suggested by Furman et al. (2004). Barrier lavas also exhibit a strong Type III signature. However, a pronounced negative Zr-Hf anomaly and mild positive Eu anomaly (also noted by Furman et al. 2004) suggests additional complexity in the origin of these lavas. Negative Zr-Hf anomalies seen in magmas elsewhere in East Africa correlate with elevated $P_2O_5$ and have been interpreted in terms of apatite in the source of these lavas (Rooney, 2020a). This interpretation is consistent with observations at Barrier, where lavas from this edifice plot at significantly elevated $P_2O_5$ in comparison with the other portions of this sector of the EARS (Fig. 4). The same pattern is observed at Rungwe (southern EARS) where Type III lavas (Rooney, 2020a) exhibit an isotopic signature consistent with a deep mantle plume (Hilton et al., 2011; Halldórsson et al., 2014) but have a clear metasomatic apatite overprint manifesting as a pronounced negative Zr-Hf anomaly (Furman, 1995; Ivanov et al., 1999). These observations suggest that Barrier magmas may have assimilated apatite enroute to the surface, likely in a metasome within the lithospheric mantle (lacking amphibole). One sample from Birds Nest also contains a negative Zr-Hf anomaly, and some samples from this edifice are interpreted to be derived from melting of an amphibole-bearing source in the lithospheric mantle (Furman et al., 2004). The origin of this apatite-bearing metasome remains unknown but it is notable that lavas with this signature exhibit radiogenic $^{206}Pb/^{204}Pb$, forming a continuum with samples from Central and North Island (Fig. 9); South Island does not fall on this continuum.

The prior observation by Furman et al. (2004) that Central Island lavas are derived from an amphibole-bearing source is consistent with the Type IV magma patterns exhibited by these samples (Fig. 4) and suggestive of a hybrid signature of plume influenced upper mantle (Type III) mixing with a metasome-derived melt (Type II). It is important to note that this metasomatic source is quite distinct from those discussed above in that it lacks evidence of apatite and has less radiogenic $^{206}Pb/^{204}Pb$ (Fig. 9). The existence of two metasomatic signatures, both with distinct isotopic fingerprints, potentially resolves an unanswered question posed in previous studies (Furman et al., 2004). The few data points available from North Island suggest a Type III pattern, though it remains unclear if apatite also affects these magmas as observed at Barrier. Korath has insufficient data available to construct a primitive mantle normalized figure, however the extreme enrichment in incompatible trace elements (e.g., Nb; Fig. 4) is suggestive of a lithospheric mantle contribution (either Type II or IV). When considered collectively, the extant data from the Quaternary volcanism associated with Lake Turkana demonstrates that magmatism is derived from diverse sources that span the lithosphere and asthenosphere; there is no clear evidence for the development of a dominantly sub-lithosphere derived magmatism like that observed in the central and northern Main Ethiopian Rift (e.g., Furman et al., 2006a; Rooney et al., 2012a). This is somewhat counterintuitive given the long history of magmatism and rifting within the Turkana Depression that extends over at least 35 Myr (Morley et al., 1999; Brown and McDougall, 2011; Boone et al., 2019).

Type III magmas from East Africa exhibit elevated He isotope ratios consistent with volatile contributions from a deeply-sourced mantle plume (Marty et al., 1993, 1996; Scarsi and Craig, 1996; Pik et al., 2006; Hilton et al., 2011; Rooney et al., 2012a; Halldórsson et al., 2014; Rooney, 2020d). $H_2O$/Ce ratios for South Island melt inclusions are highly constrained (237-264) with one outlier caused by low Ce concentrations (Fig. 8). The values are similar to that anticipated for a "C"/FOZO plume-influenced mantle (200-250: Dixon et al., 2002), consistent with the model of Type III magma generation. However, it should be noted when comparing different regions in the EARS that large heterogeneity in Ce concentrations appears to be the predominant influence on $H_2O$/Ce ratios (Fig. 8). Notably, Type V lavas from Bufumbira (Virunga), which are derived from a metasomatically-enriched lithospheric mantle, exhibit extreme depletion in $H_2O$/Ce (Fig. 8), an observation inconsistent with the suggestion by Dixon et al. (2002) that the addition of hydrous fluid phases to the mantle should increase $H_2O$/Ce in derivative melt. While some portion of the low $H_2O$/Ce at Bufumbira may result from $H_2O$ diffusive loss during both original slow cooling in lava and laboratory melt inclusion rehomogenization (Hudgins et al., 2015), Ce concentrations roughly 400% higher than Type III magmas (Fig. 8) may also point to REE-enriched nominally anhydrous phases in the metasome. Indeed, experimental results of melting of a hornblendite lithology yield lower $H_2O$/Ce (72-155: Pilet et al., 2008) than melts derived from N-MORB (~200: Dixon et al., 2002). In contrast, the significantly enriched values of $H_2O$/Ce evident at Butajira (Main Ethiopian Rift) (Fig. 8) appear related to a Ce (and other incompatible trace element) depletion of uncertain origin. Accordingly, caution should be exercised in the interpretation of $H_2O$/Ce values in East African magmas (as noted by other authors in the region, e.g., Iddon and Edmonds, 2020). Despite these complexities, for relatively undegassed melt inclusions (those over ~1800 ppm $CO_2$), it would appear that Type III magmas in East Africa contain between about 0.9 and 1.6 wt % $H_2O$ (Fig. 8). Some latitudinal heterogeneity in the $H_2O$ content of Type III magmas is also apparent, as South Island $H_2O$ concentrations are lower than those of the Main Ethiopian Rift, despite the South Island samples being typically more evolved.

### 5.2 Volatile Content of South Island and Depth of Mafic Magma Fractionation

There are limited existing datasets reporting the volatile content in olivine-hosted mafic rift lavas in East Africa, however studies from Quaternary axial volcanic centers in the Main Ethiopian Rift

(Iddon and Edmonds, 2020), Afar at Erta 'Ale (Field et al., 2012) and Nabro (Donovan et al., 2018), and the Virunga Volcanic Province at Nyamuragira (Head et al., 2011) and Bufumbira (Hudgins et al., 2015) provide suitable comparator suites for the Quaternary axial volcanic center of South Island. The pressure of melt inclusion entrapment along the modern East African Rift System has some commonalities that depend on the location of the volcanic edifice – specifically there exists a correlation between depths of magma ponding and whether a volcano is located on or off the primary axis of strain accommodation. Nabro volcano is located off-axis, along the transverse structures in Afar (Wiart and Oppenheimer, 2005; Rooney, 2020c; Donovan et al., 2018) and is inferred to have a vertically extensive magmatic plumbing system, extending from ~100 to ~500 MPa, with most melt inclusions trapped at 5-10 km depth but some extending to the base of the crust at 20 km (Donovan et al., 2018). Most of the Nabro melt inclusions do not contain vapor bubbles. The data for Nabro contrast to the very shallow crystallization pressures of the axial Erta 'Ale volcano where pressures of 7-42 MPa (0.2 – 1.4 km) have been inferred to result from very shallow crystallization in the upper 1.5 km of the magma column, consistent with the persistently active lava lake there (Field et al., 2012). Such low pressures of crystallization are seen in other volcanoes with open conduits and persistently active lava lakes (e.g., Erebus: Oppenheimer et al., 2011; Kilauea: Lerner et al., 2021).

In the Main Ethiopian Rift, strain has migrated from rift border faults to zones of focused intrusion located on the rift floor that are characterized by intense faulting, linear chains of cinder cones, and large silicic centers (Mohr, 1967; WoldeGabriel et al., 1990; Ebinger and Casey, 2001; Casey et al., 2006). The most significant of these zones of focused intrusion is the Wonji Fault Belt (WFB), which extends from Afar through the northern Main Ethiopian Rift (Mohr, 1967). The WFB extends into the central Main Ethiopian Rift, but is joined by a parallel belt of focused magmatic intrusion – the Silti-Debre Zeyit Fault Zone (SDFZ) (Rooney et al., 2011). The WFB is typically regarded as the primary belt of focused intrusuion (axial), while the SDFZ is viewed as subordinate (off-axis) (e.g., Iddon and Edmonds, 2020), though the specifics of strain accomodation in each belt are complex (Rooney et al., 2011). While both the WFB and SDFZ exhibit broadly similar morphological characteristics, mafic magmas in each system may reveal differences where magmas pond. At Kone volcano along the axial WFB in the northern Main Ethiopian Rift, storage pressures for mafic melt inclusions are <50 to 350 MPa (≤~13 km), exhibiting bimodal clustering at <100 MPa and 250-350 MPa (Iddon and Edmonds, 2020). However, these should be regarded as minimum pressures because melt inclusions with vapor bubbles were not analyzed, so the data could be biased towards lower pressure, bubble-free inclusions. At Butajira along the subordinate (or off-axis) SDFZ in the central Main Ethiopian Rift, the volatile data is more distributed than for Kone, though trapping pressures for mafic melt inclusions cover a nearly identical range, with two values extending higher to ~500 MPa (~18 km) (Iddon and Edmonds, 2020). The low-pressure mode at Kone likely is the result of some low pressure degassing-driven crystallization in the conduit system (e.g., Mordensky and Wallace, 2018). Pyroxene barometry, thermodynamic models of melt evolution, and dike self-similar clustering all suggest polybaric fractionation systems in this region, but that in volcanoes along the rift axis, magmas may rise and differentiate at shallower levels in comparison to off-axis volcanoes (Trua et al., 1999; Rooney et al., 2005, 2007; Iddon and Edmonds, 2020; Mazzarini et al., 2013). This dichotomy in the averge depth of at which magmas may pond is also consistent with magma fractionation trends – lavas from on-axis and off-axis rift sectors exhibit distinct $CaO/Al_2O_3$ and Sr patterns indicative of significant plagioclase (shallow) or pyroxene (deep) fractionation respectively (e.g., Trua et al., 1999; Peccerillo et al., 2003; Rooney et al., 2007) (Fig. 10).

Magmas represented by the melt inclusions at South Island in Turkana exhibit major and trace element similarities to magmas from the axial vocanic center of Kone in the northern Main Ethiopian Rift, and are distinct from magmas from the off-axis SDFZ in the central Main

Ethiopian Rift (Fig. 10). Given the prior discussion demonstrating that there are broadly similar mantle sources generating South Island and Quaternary MER magmas, this observation may reflect magma ponding depth similarities between South Island and axial centers in the MER. South Island volatile data exhibit vapor saturation pressures with a median value of 342 MPa (Supplemental Information), similar to the higher-pressure mode at Kone. Presuming a crustal density of ~2850 kg/m$^3$ (roughly equivalent to the middle crust assumed for Turkana from Emishaw & Abdelsalem (2019)), a conversion of ~28 MPa per kilometer is calculated, equivalent to a median magma ponding depth of ~12 km. This value virtually identical to the maximum value of ~13 km calculated for Kone (Iddon and Edmonds, 2020). These data are consistent with a broadly equivalent mafic magma plumbing system at depth for both Kone and South Island.

Establishing the plate context of this ponding depth requires independent estimates of the crustal thickness and structure. In the central Main Ethiopian Rift and Kenya Rift, active source seismic campaigns have established that crustal thickness is ~35 km (Mechie et al., 1997; Maguire et al., 2006). However, within the two broad depressions in the EARS (Turkana and Afar), crustal thickness estimates are much thinner. In the central part of the Turkana Basin under Lake Turkana, crustal thickness is ~20 km (Mechie et al., 1994). Along the northern Main Ethiopian Rift and into southern Afar, the crust progressively thins northward: ~30 km at Kone to 23-26 km-thick further north (Maguire et al., 2006; Lavayssière et al., 2018), eventually reaching 16 km in portions of the triple junction (Hammond et al., 2011). Crustal structure beneath Kone volcano in the northern Main Ethiopian Rift is dominated by a boundary between the upper and lower crust at ~10 km, defined by a change in seismic velocity from 6.4 to 6.7 km s$^{-1}$ (Maguire et al., 2006). In Turkana, the upper-lower crust boundary also occurs at ~10 km, but here separates an upper crust with a seismic velocity of 6.1 km s$^{-1}$ from the lower crust with a seismic velocity of 6.4 km s$^{-1}$ (Mechie et al., 1997). Based on these existing constraints, the lower crust at Kone (~20 km) is much thicker than that at South Island (10 km), yet the ponding depths of magmas at South Island (12 km) and Kone (13 km) are similar. However, given the transition between the lower and upper crust occurs at the same depth in both locations (10 km), it is possible that the depth of magma storage is in part controlled by crustal density, as magmas in both volcanic systems pond just below the lower to upper crust transition.

### 5.3 Implications for strain distribution

The results of this study may have implications for understanding modern strain distribution within the Turkana Depression and its relationship with the development of axial magmatism in much of the Eastern Branch of the EARS over the past 1 Myr (Rooney, 2020b). Since the Pliocene, magmatism in the Eastern Branch of the EARS has transitioned from large, basin filling eruptions of trachytic magmas towards becoming progressively more focused into linear belts of relatively small-volume bi-modal magmatism (Mohr, 1967; Rooney et al., 2011; Rooney, 2020b). The development of these linear belts was concomitant with the migration of strain towards these new intra-rift axes of extension (Boccaletti et al., 1998; Hayward and Ebinger, 1996; Ebinger and Casey, 2001; Casey et al., 2006). However, the existence of overlapping intra-rift axes may create ambiguity in interpreting the current locus of strain in some parts of the EARS (e.g., Rooney et al., 2011).

In the Main Ethiopian Rift, the relative Nubia-Somalia plate velocity is accommodated by extension that is a function of two distinct components: (A) distributed strain within the Ethiopian highlands, and (B) focused strain within the rift (Stamps et al., 2008, 2018; Birhanu et al., 2016; Knappe et al., 2020). While some strain continues to be accommodated on the rift border faults (Pizzi et al., 2006; Agostini et al., 2011; Molin and Corti, 2015), the extension is preferentially accommodated in zones of focused magmatic-tectonic activity within the rift (e.g., Bilham et al., 1999). Where these zones of focused magmatic-tectonic activity overlap, one zone may become dominant over the other, resulting in what is termed ‘axial’ systems that are characterized by largely shallow fractionation of sub-lithosphere derived magmas, whereas the sub-ordinate belt (off-axis) is characterized by magmatism that experiences a greater degree of deeper fractionation (Rooney, 2010; Rooney et al., 2011; Iddon and Edmonds, 2020). Shallow fractionation, attributed to a more well-developed magma plumbing system, results from a greater magma flux into the lithosphere that is able to generate greater magma overpressure to overcome the surrounding lithospheric stresses (Rubin, 1990; Parsons and Thompson, 1991). This greater magma flux into the lithosphere adds volume to the lithosphere in greater proportion than at a less well-developed magma plumbing system, thereby accommodating more strain (Rubin and Pollard, 1988; Rooney et al., 2014).

Pliocene to recent magmatism in Turkana exhibits some of the same styles of magmatic activity to that of the narrow rifts to the north (Main Ethiopian Rift) and south (Kenya Rift) (Rooney, 2020b). Notably, large volume relatively evolved lavas of the Pliocene Gombe Stratoid Series (Hackman, 1988; Key and Watkins, 1988; Haileab et al., 2004) were followed by shield volcanoes (Key et al., 1987; Ochieng et al., 1988; Furman et al., 2006b; Gathogo et al., 2008), and then with modern small volume basaltic cinder cones occurring along linear alignments (Fig. 2) (Class et al., 1994; Furman et al., 2004; Corti et al., 2019; Rooney, 2020b).2) Modern magmatism associated with these cinder cone belts is distributed into two regions – magmatism associated with Lake Turkana (Karson and Curtis, 1994; Furman et al., 2004; Brown and Carmichael, 1971, 1969), and that occurring to the east of the Lake (Fig. 2) (Key et al., 1987; Ebinger et al., 2000; Shinjo et al., 2011; Corti et al., 2019; Franceschini et al., 2020). The Lake Turkana Basin (Fig. 2) has recently been suggested to represent the axial linkage region between the Kenya Rift and Main Ethiopian Rift – a process that has been hypothesized to have initiated in the Pliocene (Corti et al., 2019). The inference that the Lake Turkana Basin is currently being impacted by strain focusing and rifting processes is consistent with historical or very young volcanism reported for this area in both the south (von Höhnel, 1894) and north of the Basin (Jicha and Brown, 2014). However, the presence of zero aged $^{40}Ar/^{39}Ar$ dates for volcanism located east of the Turkana Basin (Franceschini et al., 2020) make it apparent that there are at least two zones of magmatic activity in the Turkana Depression that are active contemporaneously. Might this suggest, as in the central Main Ethiopian Rift, a more complex evolution of strain accommodation? Existing structural studies instead suggest that volcanic vents located east of the Lake are unrelated to regional extension – the vents exhibit alignments that are at a high-angle to rift-related faults and developed after the abandonment of the rift in that region (Corti et al., 2019; Franceschini et al., 2020).

Geodetic constraints within the Turkana Basin add further clarity as to the modern loci of strain and show a strong correlation between the presence of magmatism and extension in the Lake Turkana Basin. Along the northern portions of Turkana, extensional strain is broadly distributed with a component occurring within the Omo basin or Ethiopian Highlands, and also the Chew Bahir/Teltele Plateau (Fig. 2) (Knappe et al., 2020) for a total rate of 4.4 mm/year, consistent with existing regional models (Stamps et al., 2008; Saria et al., 2013). Current GPS extension rates in Southern Turkana are estimated to be 4.7 ± 0.4 mm/yr, with extensional strain focused in a ~20-30 km wide zone (Knappe et al., 2020). These values are consistent with time-average Holocene extension rates of 3.5-5.8 mm/yr estimated from reflection seismic analysis of axial normal faults in South Turkana basin, which are aligned with South Island volcano (Muirhead et al., this volume). In all, these observations suggest that the locus of extensional strain at this latitude is currently centered around South Island. Combined analysis of both single- and multi-channel seismic data, considered in the context of the evolving lake stratigraphy (Feibel, 2011; Nutz et al., 2020), also suggest that this transition to focused axial extension likely initiated in the Late Pleistocene (Muirhead et al., this volume) and later than similar transitions observed farther north in the Main Ethiopian Rift (Boccaletti et al., 1998; Ebinger and Casey, 2001; Wolfenden et al., 2004).

These geodetic and structural observations suggesting that the Lake Turkana Basin is the current locus of strain supports the results of this study. At South Island, the occurrence of sub-lithospheric derived Type III magmas and a crustal differentiation system that resembles that of the axial systems from the Main Ethiopian Rift is consistent with the Lake Turkana Basin being the current axial sector of the rift. In contrast, magmatism to the east of the Turkana basin contains abundant mantle nodules (e.g., Conticelli et al., 1999; Casagli et al., 2017; Orlando et al., 2006) with a very immature magmatic system that undergoes little crustal fractionation (Franceschini et al., 2020). These observations further reveal that the development of axial magmatism in Lake Turkana also occurred during a period of extensional strain focusing into the axial fault system, suggesting that strain localization was intimately linked with evolving magmatic processes in the region.

## 6. Conclusions

Lavas at South Island represent melts of the upper mantle beneath the Turkana Depression. These lavas are compositionally equivalent to Quaternary axial magmas from along the Eastern Branch of the East African Rift System and are interpreted as a melt of a plume-influenced upper mantle. The volatile element systematics of South Island show that bubble-corrected $CO_2$ concentrations are also similar to other Quaternary axial volcanoes within the East African Rift System and magma ponding occurred at depths of ~12 km. We interpret these data in the context of new structural constraints (Muirhead et al., this volume) to suggest that South Island represents a zone of focused tectonic-magmatic extension similar to those identified within the Main Ethiopian Rift (e.g., Ebinger and Casey, 2001). Moreover, when considered within the regional geodetic framework (e.g., Knappe et al., 2020), it is apparent that the modern partitioning of strain in the Turkana Depression, at this latitude, occurs in the Lake Turkana Basin.

## Acknowledgements

Mary Grace Owens is thanked for contributions to the data collection, processing and interpretation as part of an undergraduate research project. We would like to thank Christina Cauley and Lissie Connors for assistance with melt inclusion corrections. We thank Raffaello Cioni and Giacomo Corti for their constructive peer reviews. Nick Varley is thanked for his editorial handling.

## Funding

This work was supported by US National Science Foundation Grants: EAR 1551872 and OCE 1850606 to Rooney, EAR 1654518 to Muirhead.

## Data Availability

All data generated or analyzed during this study are included in this article (and its supplementary information files).

## Figure Captions:

Figure 1: Map showing the location of South Island relative to other Quaternary volcanic centers in the East African Rift System. Place names mentioned in the text are also shown on this figure. Features are adapted from the maps presented in Rooney (2020b, 2020a, 2020c).

Figure 2: Regional map of the Turkana Depression and surrounding areas. Volcanic features are shown in yellow, tectonic features are shown in italics as off-white. The extent of volcanic activity from the Stratoid Phase until present is also shown. Shapes adapted from the maps presented in Rooney (2020b, 2020a, 2020c) which were compiled from other sources (Kazmin et al., 1981; Haileab et al., 2004; Guth, 2013; Erbello and Kidane, 2018), and also from Franceschini et al. (2020). Note that all volcanics of the Huri Hills (including Quaternary cones) are subsumed into a single unit.

Figure 3:

A. Modified version of the map of South Island presented by Karson & Curtis 1994. Mapped geologic units of South Island are: S1 – Basaltic flows, pillow lavas, and hyaloclastites; S2 – Undifferentiated, massive, poorly-sorted light olive-brown tuffs; S3 – Undifferentiated tan to gold, massive to fine bedded tuffs and lapilli-tuffs with subordinate aggluntinate; S4 – Undifferentiated basaltic lavas; S5 – Fine, black to reddish-gray ash. Map was overlain on ESRI World Hill Shade basemap that used the following sources: Esri, Airbus DS, USGS, NGA, NASA, CGIAR, N Robinson, NCEAS, NLS, OS, NMA, Geodatastyrelsen, Rijkswaterstaat, GSA, Geoland, FEMA, Intermap, and the GIS user community. The map has been simplified and cones associated with S4 have been subsumed.

B. 3D image of South Island with the units from part A. above shown draped over Google Satellite imagery © 2021 Maxar Technologies and rendered into 3D with a NASA SRTM DEM with a 1.5x vertical exaggeration using QGIS and QGIS2threejs plugin. North arrow shows in red on lower left.

Figure 4: Variation of major and trace elements for the Quaternary volcanic centers in the Lake Turkana Basin. Data sources are: Barrier (Brown and Carmichael, 1971; Koyaguchi, 1984; Tatsumi and Kimura, 1991; Rogers et al., 2000, 2006; MacDonald et al., 2001; Kabeto et al., 2001; Furman et al., 2004); Birds Nest and Central Island (Furman et al., 2004); Korath (Brown and Carmichael, 1969); North Island (Brown and Carmichael, 1971; Bloomer et al., 1989; Furman et al., 2004); South Island (existing) (Brown and Carmichael, 1971; Furman et al., 2004). The data show the relatively wide distribution range in $P_2O_5$ but strong correlation in other major elements. Incompatible trace elements show a significant enrichment in Korath samples in Nb and La. Ba is enriched for Korath samples and some Barrier and Bird's Nest samples. Whole rock chondrite normalized (CN) La/Yb values for South Island vary from 4.6 to 10.6; melt inclusions occupy the lower part of this range (4.4-5.7) but also include an anomalously low value from MI-7a of 2.9 (discussed in the main text). Our new whole rock and melt inclusion data plot among the existing South Island whole rock data and are presented in the supplementary information.

Figure 5: Chondrite normalized rare earth element values (Boynton, 1984) for the Quaternary volcanic centers in the Lake Turkana Basin. Data sources are the same as for Figure 4. The Korath dataset lacks sufficient rare earth element data to construct this plot. South Island melt inclusions plot among the existing regional data with the exception of the one sample noted in the main text to have a depletion in the most incompatible rare earth elements. The grey background lines represent the full dataset that is shown on this figure and provides a comparison between each unit and the overall dataset.

Figure 6: Primitive mantle normalized values (Sun and McDonough, 1989) for the Quaternary volcanic centers in the Lake Turkana Basin. Data sources are the same as for Figure 4. The Korath dataset lacks sufficient rare earth element data to construct this plot. New South Island data show the strong Type III magma pattern in both the whole rock and melt inclusion data. Barrier shows a similar pattern but with a strong negative Zr-Hf anomaly indicative of interaction with a metasomatic source. Similarly, Central Island shows a Type IV lava pattern that is indicative of interaction with the lithospheric mantle. The grey background lines represent the full dataset that is shown on this figure and provides a comparison between each unit and the overall dataset.

Figure 7: High precision olivine minor and trace element data for South Island compared with other datasets: MORB, Afar, Within Plate Basalt (WPM – thick) (Sobolev et al., 2007);

Ugandites (Foley et al., 2011); Melanephelinite, basanite, and alkali basalts are from the Miocene Gerba Guracha Shield volcano on the Ethiopian highlands (Rooney et al., 2017); Ethiopian Flood Basalt (Rooney et al., 2017). South Island data are distinct from olivine derived from metasomatically enriched sources. The low Cr values in South Island olivine in comparison to the other datasets is notable.

Figure 8: Melt inclusion volatile data plotted versus MgO and other elements for olivine-hosted mafic melt inclusions from the East African Rift System for more mafic magmas (<55 wt. % $SiO_2$). The volatile data include both experimentally rehomogenized and naturally quenched glasses and are discussed in the main text. $H_2O$/Ce is used as a measure of the relative enrichment of the mantle source in $H_2O$ (e.g., Dixon et al., 2002). For East African Rift System lavas derived from metasomatic sources, the Ce concentration of the mantle source is the dominant control on the $H_2O$/Ce values. Where reported, MgO is the post entrapment crystallization (PEC) corrected value of the melt inclusion. Data for South Island are bubble-corrected. Aluto, Butajira, and Kone are from the Main Ethiopian Rift (Iddon and Edmonds, 2020); Bufumbira and Nyamuragira are from the Virunga Volcanic Province from the Western Branch of the East African Rift System and are derived from a metasomatically enriched source in the lithospheric mantle (Head et al., 2011; Hudgins et al., 2015); Nabro and Erta 'Ale volcanoes are in Afar (Field et al., 2012; Donovan et al., 2018).

Figure 9: Variation in Quaternary volcanic centers in the Lake Turkana Basin of $^{206}Pb/^{204}Pb$ with an indicator of a source with metasomatic amphibole denoted by low primitive mantle normalized (Sun and McDonough, 1989) ratio of Hf/Sm. All data, including South Island, are from existing publications (MacDonald et al., 2001; Furman et al., 2004; Rogers et al., 2006). Note the continuum between Barrier, North Island, and Central Island in terms of isotopic ratios and an indicator of metasomatic enrichment. It is also apparent that South Island does not fall on this continuum, consistent with the hypothesis of a sub-lithospheric origin for these lavas.

Figure 10: Co-variation of whole-rock $CaO/Al_2O_3$ and Sr (ppm) with MgO in the Wonjii Fault Belt (WFB), Silti-Debre Zeyit Fault Zone (SDFZ), and South Island melt inclusion data. The distinction between the SDFZ and WFB data is interpreted in terms of a greater proportion of clinopyroxene fractionation at deeper levels within the crust in the SDFZ, in comparison to the WFB where plagioclase is more dominant at shallower levels (e.g., Rooney et al., 2005, 2007). The South Island melt inclusion data plot with the WFB data, suggesting a fractionation of a mineral assemblage with a greater proportion of plagioclase. Data sources for the WFB and SDFZ are fully presented elsewhere (Rooney, 2020b).

Figure 11: Volatile element variation for East African melt inclusions overlain on an isobar volatile saturation grid derived from VolatileCalc 1.1 (Newman and Lowenstern, 2002). Model conditions assumed 48.5 % $SiO_2$ at 1115°C, the average for the South Island melt inclusions. Volatile data for South Island is presented as bubble corrected, however we also show the uncorrected data. Data sources are the same as Figure 8.

## 7. References

Agostini, A., Bonini, M., Corti, G., Sani, F., Manetti, P., 2011. Distribution of Quaternary deformation in the central Main Ethiopian Rift, East Africa. Tectonics 30, TC4010. https://doi.org/10.1029/2010tc002833

Autin, J., Bellahsen, N., Husson, L., Beslier, M.-O., Leroy, S., d'Acremont, E., 2010. Analog models of oblique rifting in a cold lithosphere. Tectonics 29.

Ayele, A., Keir, D., Ebinger, C., Wright, T.J., Stuart, G.W., Buck, W.R., Jacques, E., Ogubazghi, G., Sholan, J., 2009. September 2005 mega-dike emplacement in the Manda-Harraro nascent oceanic rift (Afar depression). Geophys. Res. Lett. 36, L20306. https://doi.org/10.1029/2009gl039605

Baker, J., Snee, L., Menzies, M., 1996. A brief Oligocene period of flood volcanism in Yemen: Implications for the duration and rate of continental flood volcanism at the Afro-Arabian triple junction. Earth Planet. Sci. Lett. 138, 39–55.

Bastow, I.D., Keir, D., 2011. The protracted development of the continent-ocean transition in Afar. Nat. Geosci. 4, 248–250. https://doi.org/10.1038/Ngeo1095

Behn, M.D., Buck, W.R., Sacks, I.S., 2006. Topographic controls on dike injection in volcanic rift zones. Earth Planet. Sci. Lett. 246, 188–196. https://doi.org/DOI 10.1016/j.epsl.2006.04.005

Belachew, M., Ebinger, C., Coté, D., 2012. Source mechanisms of dike-induced earthquakes in the Dabbahu-Manda Hararo rift segment in Afar, Ethiopia: implications for faulting above dikes. Geophys. J. Int. 192, 907–917.

Benoit, M.H., Nyblade, A.A., Pasyanos, M.E., 2006. Crustal thinning between the Ethiopian and East African plateaus from modeling Rayleigh wave dispersion. Geophys. Res. Lett. 33, L13301, doi: 10.1029/2006gl025687. https://doi.org/Artn L13301 Doi 10.1029/2006gl025687

Beutel, E., van Wijk, J., Ebinger, C., Keir, D., Agostini, A., 2010. Formation and stability of magmatic segments in the Main Ethiopian and Afar rifts. Earth Planet. Sci. Lett. 293, 225–235. https://doi.org/DOI 10.1016/j.epsl.2010.02.006

Bialas, R.W., Buck, W.R., Qin, R., 2010. How much magma is required to rift a continent? Earth Planet. Sci. Lett. 292, 68–78. https://doi.org/doi:10.1016/j.epsl.2010.01.021

Bilham, R., Bendick, R., Larson, K., Mohr, P., Braun, J., Tesfaye, S., Asfaw, L., 1999. Secular and tidal strain across the main Ethiopian rift. Geophys. Res. Lett. 26, 2789–2792.

Birhanu, Y., Bendick, R., Fisseha, S., Lewi, E., Floyd, M., King, R., Reilinger, R., 2016. GPS constraints on broad scale extension in the Ethiopian Highlands and Main Ethiopian Rift. Geophys. Res. Lett. 43, 6844–6851.

Bloomer, S.H., Curtis, P.C., Karson, J.A., 1989. Geochemical variation of Quaternary basaltic volcanics in the Turkana Rift, northern Kenya. J. Afr. Earth Sci. Middle East 8, 511–532.

Boccaletti, M., Bonini, M., Mazzuoli, R., Abebe, B., Piccardi, L., Tortorici, L., 1998. Quaternary oblique extensional tectonics in the Ethiopian Rift (Horn of Africa). Tectonophysics 287, 97–116.

Boone, S.C., Kohn, B.P., Gleadow, A.J., Morley, C.K., Seiler, C., Foster, D.A., 2019. Birth of the East African Rift System: Nucleation of magmatism and strain in the Turkana Depression. Geology 47, 886–890.

Bosworth, W., 1992. Mesozoic and Early Tertiary Rift Tectonics in East-Africa. Tectonophysics 209, 115–137.

Bosworth, W., Morley, C.K., 1994. Structural and stratigraphic evolution of the Anza rift, Kenya. Tectonophysics 236, 93–115.

Boynton, W.V., 1984. Cosmochemistry of the rare earth elements: meteorite studies, in: Henderson, P. (Ed.), Rare Earth Element Geochemistry. Elsevier, Amsterdam, pp. 63–114.

Brown, F.H., Carmichael, I.S.E., 1971. Quaternary volcanoes of the Lake Rudolf region: II. The lavas of North Island, South Island and the Barrier. Lithos 4, 305–323.

Brown, F.H., Carmichael, I.S.E., 1969. Quaternary volcanoes of the Lake Rudolf region: 1. The basanite-tephrite series of the Korath Range. Lithos 2, 239–260.

Brown, F.H., McDougall, I., 2011. Geochronology of the Turkana depression of northern Kenya and southern Ethiopia. Evol. Anthropol. Issues News Rev. 20, 217–227.

Brune, S., Corti, G., Ranalli, G., 2017. Controls of inherited lithospheric heterogeneity on rift linkage: Numerical and analog models of interaction between the Kenyan and Ethiopian rifts across the Turkana depression. Tectonics 36, 1767–1786.

Buck, W.R., 2006. The role of magma in the development of the Afro-Arabian rift system, in: Yirgu, G., Ebinger, C., Maguire, P. (Eds.), The Afar Volcanic Province within the East African Rift System. Special Publication of the Geological Society, London, pp. 43–54.

Casagli, A., Frezzotti, M.L., Peccerillo, A., Tiepolo, M., De Astis, G., 2017. (Garnet)-spinel peridotite xenoliths from Mega (Ethiopia): Evidence for rejuvenation and dynamic thinning of the lithosphere beneath the southern Main Ethiopian Rift. Chem. Geol. 455, 231–248.

Casey, M., Ebinger, C., Keir, D., Gloaguen, R., Mohamed, F., 2006. Strain accomodation in transitional rifts: Extension by magma intrusion and faulting in Ethiopian rift magmatic segments, in: Yirgu, G., Ebinger, C., Maguire, P. (Eds.), The Afar Volcanic Province within the East African Rift System. Geological Society, London, London, pp. 143–164.

Chorowicz, J., 2005. The east African rift system. J. Afr. Earth Sci. 43, 379–410.

Class, C., Altherr, R., Volker, F., Eberz, G., Mcculloch, M.T., 1994. Geochemistry of Pliocene to Quaternary alkali basalts from the Huri Hills, Northern Kenya. Chem. Geol. 113, 1–22.

Conticelli, S., Sintoni, M.F., Abebe, T., Mazzarini, F., Manetti, P., 1999. Petrology and geochemistry of ultramafic xenoliths and host lavas from the Ethiopian Volcanic Province; an insight into the upper mantle under eastern Africa. Acta Vulcanol. 11, 143–159.

Corti, G., Cioni, R., Franceschini, Z., Sani, F., Scaillet, S., Molin, P., Isola, I., Mazzarini, F., Brune, S., Keir, D., Erbello, A., Muluneh, A., Illsley-Kemp, F., Glerum, A., 2019. Aborted propagation of the Ethiopian rift caused by linkage with the Kenyan rift. Nat. Commun. 10, 1309. https://doi.org/10.1038/s41467-019-09335-2

Davidson, A., 1983. The Omo River Project: Reconnaissance geology and geochemistry of parts of Illubabor, Kefa, Gemu Gofa, and Sidamo. Ethiop. Inst. Geol. Surv. Bull. 2, 1–89.

Dixon, J.E., Leist, L., Langmuir, C., Schilling, J.G., 2002. Recycled dehydrated lithosphere observed in plume-influenced mid-ocean-ridge basalt. Nature 420, 385–389.

Donovan, A., Blundy, J., Oppenheimer, C., Buisman, I., 2018. The 2011 eruption of Nabro volcano, Eritrea: perspectives on magmatic processes from melt inclusions. Contrib. Mineral. Petrol. 173, 1.

Dunkelman, T.J., Karson, J.A., Rosendahl, B.R., 1988. Structural style of the Turkana rift, Kenya. Geology 16, 258–261.

Dunkley, P.N., Smith, M., Allen, D.J., Darling, W.G., 1993. The geothermal activity and geology of the northern sector of the Kenya Rift Valley.

Ebinger, C., Ayele, A., Keir, D., Rowland, J., Yirgu, G., Wright, T., Belachew, M., Hamling, I., 2010. Length and Timescales of Rift Faulting and Magma Intrusion: The Afar Rifting Cycle from 2005 to Present. Annu. Rev. Earth Planet. Sci. Vol 38 38, 439–466. https://doi.org/DOI 10.1146/annurev-earth-040809-152333

Ebinger, C.J., 1989. Tectonic development of the western branch of the East-African rift system. Geol. Soc. Am. Bull. 101, 885–903.

Ebinger, C.J., Casey, M., 2001. Continental breakup in magmatic provinces: An Ethiopian example. Geology 29, 527–530.

Ebinger, C.J., Ibrahim, A., 1994. Multiple Episodes of Rifting in Central and East-Africa - a Reevaluation of Gravity-Data. Geol. Rundsch. 83, 689–702.

Ebinger, C.J., Yemane, T., Harding, D.J., Tesfaye, S., Kelley, S., Rex, D.C., 2000. Rift deflection, migration, and propagation: Linkage of the Ethiopian and Eastern rifts, Africa. Geol. Soc. Am. Bull. 112, 163–176.

Ebinger, C.J., Yemane, T., WoldeGabriel, G., Aronson, J.L., Walter, R.C., 1993. Late Eocene-Recent volcanism and faulting in the southern main Ethiopian Rift. J. Geol. Soc. Lond. 150, 99–108.

Emishaw, L., Abdelsalam, M.G., 2019. Development of late Jurassic-early Paleogene and Neogene-Quaternary rifts within the Turkana Depression, East Africa from satellite gravity data. Tectonics 38, 2358–2377.

Erbello, A., Kidane, T., 2018. Timing of volcanism and initiation of rifting in the Omo-Turkana depression, southwest Ethiopia: Evidence from paleomagnetism. J. Afr. Earth Sci. 139, 319–329.

Feibel, C.S., 2011. A geological history of the Turkana Basin. Evol. Anthropol. Issues News Rev. 20, 206–216.

Field, L., Barnie, T., Blundy, J., Brooker, R.A., Keir, D., Lewi, E., Saunders, K., 2012. Integrated field, satellite and petrological observations of the November 2010 eruption of Erta Ale. Bull. Volcanol. 74, 2251–2271.

Foley, S.F., Jacob, D.E., O'Neill, H.S.C., 2011. Trace element variations in olivine phenocrysts from Ugandan potassic rocks as clues to the chemical characteristics of parental magmas. Contrib. Mineral. Petrol. 162, 1–20.

Franceschini, Z., Cioni, R., Scaillet, S., Corti, G., Sani, F., Isola, I., Mazzarini, F., Duval, F., Erbello, A., Muluneh, A., 2020. Recent volcano-tectonic activity of the Ririba rift and the evolution of rifting in South Ethiopia. J. Volcanol. Geotherm. Res. 403, 106989.

Furman, T., 1995. Melting of metasomatized subcontinental lithosphere - Undersaturated mafic lavas from Rungwe, Tanzania. Contrib. Mineral. Petrol. 122, 97–115.

Furman, T., Bryce, J.G., Karson, J., Iotti, A., 2004. East African Rift System (EARS) plume structure: Insights from quaternary mafic lavas of Turkana, Kenya. J. Petrol. 45, 1069–1088.

Furman, T., Bryce, J.G., Rooney, T., Hanan, B.B., Yirgu, G., Ayalew, D., 2006a. Heads and tails: 30 million years of the Afar plume, in: Yirgu, G., Ebinger, C., Maguire, P. (Eds.), The Afar Volcanic Province within the East African Rift System. Special Publication of the Geological Society, London, pp. 95–120.

Furman, T., Kaleta, K.M., Bryce, J.G., Hanan, B.B., 2006b. Tertiary mafic lavas of Turkana, Kenya: Constraints on East African plume structure and the occurrence of high-mu volcanism in Africa. J. Petrol. 47, 1221–1244.

Garcin, Y., Melnick, D., Strecker, M.R., Olago, D., Tiercelin, J.-J., 2012. East African mid-Holocene wet–dry transition recorded in palaeo-shorelines of Lake Turkana, northern Kenya Rift. Earth Planet. Sci. Lett. 331, 322–334.

Gathogo, P.N., Brown, F.H., McDougall, I., 2008. Stratigraphy of the Koobi Fora Formation (Pliocene and Pleistocene) in the Loiyangalani region of northern Kenya. J. Afr. Earth Sci. 51, 277–297.

George, R., Rogers, N., Kelley, S., 1998. Earliest magmatism in Ethiopia: Evidence for two mantle plumes in one flood basalt province. Geology 26, 923–926.

Guth, A.L., 2013. Spatial and Temporal Evolution of the Volcanics and Sediments of the Kenya Rift. Michigan Technological University.

Hackman, B.D., 1988. Geology of the Baringo-Laikipia area: degree sheet 35 with coloured 1: 250,000 geological map and results of geochemical exploration. Ministry of Environment and Natural Resources, Mines and Geological Deptartment.

Haileab, B., Brown, F.H., McDOUGALL, I., Gathogo, P.N., 2004. Gombe Group basalts and initiation of Pliocene deposition in the Turkana depression, northern Kenya and southern Ethiopia. Geol. Mag. 141, 41–53.

Halldórsson, S.A., Hilton, D.R., Scarsi, P., Abebe, T., Hopp, J., 2014. A common mantle plume source beneath the entire East African Rift System revealed by coupled helium-neon systematics. Geophys. Res. Lett. 41, 2304–2311.

Hammond, J.O.S., Kendall, J.M., Stuart, G.W., Keir, D., Ebinger, C., Ayele, A., Belachew, M., 2011. The nature of the crust beneath the Afar triple junction: Evidence from receiver functions. Geochem. Geophys. Geosystems 12, Q12004, doi:10.1029/2011gc003738. https://doi.org/10.1029/2011gc003738

Hayward, N.J., Ebinger, C.J., 1996. Variations in the along-axis segmentation of the Afar Rift system. Tectonics 15, 244–257.

Head, E.M., Shaw, A.M., Wallace, P.J., Sims, K.W., Carn, S.A., 2011. Insight into volatile behavior at Nyamuragira volcano (DR Congo, Africa) through olivine-hosted melt inclusions. Geochem. Geophys. Geosystems 12, Q0AB11. https://doi.org/10.1029/2011GC003699

Hendrie, D.B., Kusznir, N.J., Morley, C.K., Ebinger, C.J., 1994. Cenozoic extension in Northern Kenya - A quantitative model of rift basin development in the Turkana region. Tectonophysics 236, 409–438.

Hilton, D.R., Halldórsson, S.A., Barry, P.H., Fischer, T.P., de Moor, J.M., Ramirez, C.J., Mangasini, F., Scarsi, P., 2011. Helium isotopes at Rungwe Volcanic Province, Tanzania, and the origin of East African Plateaux. Geophys. Res. Lett. 38, L21304. https://doi.org/10.1029/2011GL049589

Hudgins, T.R., Mukasa, S.B., Simon, A.C., Moore, G., Barifaijo, E., 2015. Melt inclusion evidence for CO2-rich melts beneath the western branch of the East African Rift: implications for long-term storage of volatiles in the deep lithospheric mantle. Contrib. Mineral. Petrol. 169, 1–18. https://doi.org/10.1007/s00410-015-1140-9

Iddon, F., Edmonds, M., 2020. Volatile-rich magmas distributed through the upper crust in the Main Ethiopian Rift. Geochem. Geophys. Geosystems 21, e2019GC008904. https://doi.org/10.1029/2019GC008904

Illsley-Kemp, F., Keir, D., Bull, J.M., Gernon, T.M., Ebinger, C., Ayele, A., Hammond, J.O., Kendall, J.-M., Goitom, B., Belachew, M., 2018. Seismicity during continental breakup in the Red Sea rift of Northern Afar. J. Geophys. Res. Solid Earth 123, 2345–2362.

Ivanov, A.V., Rasskazov, S.V., Boven, A., Punzalan, L., Brandt, I.S., Brandt, S.B., Fernandez-Alonso, M., 1999. Timing and Late Cenozoic volcanic activity and rift basin formations in the Rungwe province of Tanzania substantiated by K–Ar and 40Ar/39Ar dating. Proc. Rift. Intracont. Setting Baikal Rift Syst. Cont. Rifts 22–30.

Jicha, B.R., Brown, F.H., 2014. An age for the Korath Range, Ethiopia and the viability of 40Ar/39Ar dating of kaersutite in Late Pleistocene volcanics. Quat. Geochronol. 21, 53–57.

Kabeto, K., Sawada, Y., Iizumi, S., Wakatsuki, T., 2001. Mantle sources and magma–crust interactions in volcanic rocks from the northern Kenya rift: geochemical evidence. Lithos 56, 111–139. https://doi.org/10.1016/S0024-4937(00)00063-3

Karson, J.A., Curtis, P.C., 1994. Quaternary volcanic centres of the Turkana Rift, Kenya. J. Afr. Earth Sci. 18, 15–35. http://dx.doi.org/10.1016/0899-5362(94)90051-5

Kazmin, V., Berhe, S.M., Wondm-Agennehu, B., 1981. Geological map of the Ethiopian Rift.

Keir, D., Ebinger, C.J., Stuart, G.W., Daly, E., Ayele, A., 2006. Strain accommodation by magmatism and faulting as rifting proceeds to breakup: Seismicity of the northern Ethiopian rift. J. Geophys. Res.-Solid Earth 111, B05314. https://doi.org/10.1029/2005jb003748

Keranen, K., Klemper, S.L., Gloaguen, R., EAGLE Working Grp, 2004. Three-dimensional seismic imaging of a protoridge axis in the Main Ethiopian rift. Geology 32, 949–952.

Key, R.M., Rop, B.P., Rundle, C.C., 1987. The development of the late Cenozoic alkali basaltic Marsabit Shield-Volcano, Northern Kenya. J. Afr. Earth Sci. 6, 475–491.

Key, R.M., Watkins, R.T., 1988. Geology of the Sabarei area. Repub. Kenya Minist. Environ. Nat. Resour. Mines Geol. Dep. Rep. 111.

Knappe, E., Bendick, R., Ebinger, C., Birhanu, Y., Lewi, E., Floyd, M., King, R., Kianji, G., Mariita, N., Temtime, T., 2020. Accommodation of East African Rifting across the Turkana Depression. J. Geophys. Res. Solid Earth 125, e2019JB018469.

Koptev, A., Gerya, T., Calais, E., Leroy, S., Burov, E., 2018. Afar triple junction triggered by plume-assisted bi-directional continental break-up. Sci. Rep. 8, 1–7.

Koyaguchi, T., 1984. Volcanic Rocks in the Samburu Hills, Northern Kenya. Afr. Study Monograhs 2, 147–179.

Krans, S.R., Rooney, T.O., Kappelman, J., Yirgu, G., Ayalew, D., 2018. From initiation to termination: a petrostratigraphic tour of the Ethiopian Low-Ti Flood Basalt Province. Contrib. Mineral. Petrol. 173, 37. https://doi.org/10.1007/s00410-018-1460-7

Lavayssière, A., Rychert, C., Harmon, N., Keir, D., Hammond, J.O.S., Kendall, J.-M., Doubre, C., Leroy, S., 2018. Imaging Lithospheric Discontinuities Beneath the Northern East African Rift Using S-to-P Receiver Functions. Geochem. Geophys. Geosystems 19, 4048–4062. https://doi.org/10.1029/2018GC007463

Le Gall, B., Daoud, M.A., Maury, R.C., Rolet, J., Guillou, H., Sue, C., 2010. Magma-driven antiform structures in the Afar rift: the Ali Sabieh range, Djibouti. J. Struct. Geol. 32, 843–854.

Le Gall, B., Vétel, W., Morley, C.K., 2005. Inversion tectonics during continental rifting: The Turkana Cenozoic rifted zone, northern Kenya. Tectonics 24.

Le Maitre, R.W., 2002. Igneous Rocks - A classification and glossary of terms. Cambridge University Press, Cambridge, U.K.

Lerner, A.H., Wallace, P.J., Shea, T., Mourey, A.J., Kelly, P.J., Nadeau, P.A., Elias, T., Kern, C., Clor, L.E., Gansecki, C., 2021. The petrologic and degassing behavior of sulfur and other magmatic volatiles from the 2018 eruption of Kīlauea, Hawaiʻi: melt concentrations, magma storage depths, and magma recycling. Bull. Volcanol. 83, 1–32.

MacDonald, R., Rogers, N.W., Fitton, J.G., Black, S., Smith, M., 2001. Plume-lithosphere interactions in the generation of the basalts of the Kenya Rift, East Africa. J. Petrol. 42, 877–900.

Macgregor, D., 2015. History of the development of the East African Rift System: A series of interpreted maps through time. J. Afr. Earth Sci. 101, 232–252.

Mackenzie, G., Thybo, H., Maguire, P., 2005. Crustal velocity structure across the Main Ethiopian Rift: Results from 2-dimensional wide-angle seismic modelling. Geophys. J. Int. 162, 994–1006.

Maguire, P., Keller, G.R., Klemper, S.L., Mackenzie, G., Keranen, K., Harder, S., O'Reilly, B., Thybo, H., Asfaw, L., Kahn, M., Amha, M., 2006. Crustal structure of the Northern Main Ethiopian Rift from the EAGLE controlled source survey; a snapshot of incipient lithospheric break-up, in: Yirgu, G., Ebinger, C., Maguire, P. (Eds.), The Afar Volcanic Province within the East African Rift System. Special Publication of the Geological Society, London, pp. 269–292.

Manighetti, I., Tapponnier, P., Courtillot, V., Gallet, Y., Jacques, E., Gillot, P.Y., 2001. Strain transfer between disconnected, propagating rifts in Afar. J. Geophys. Res.-Solid Earth 106, 13613–13665.

Mariita, N.O., Keller, G.R., 2007. An integrated geophysical study of the northern Kenya rift. J. Afr. Earth Sci. 48, 80–94.

Marty, B., Appora, I., Barrat, J.-A.A., Deniel, C., Vellutini, P., Vidal, P., Kusakabe, M., Shinohara, H., 1993. He, Ar, Sr, Nd and Pb isotopes in volcanic rocks from Afar; evidence for a primitive mantle component and constraints on magmatic sources. Geochem. J. 27, 219–228.

Marty, B., Pik, R., Gezahegn, Y., 1996. Helium isotopic variations in Ethiopian plume lavas; nature of magmatic sources and limit on lower mantle contribution. Earth Planet. Sci. Lett. 144, 223–237.

Mazzarini, F., Rooney, T.O., Isola, I., 2013. The intimate relationship between strain and magmatism: A numerical treatment of clustered monogenetic fields in the Main Ethiopian Rift. Tectonics 32, 49–64. https://doi.org/10.1029/2012tc003146

Mechie, J., Keller, G.R., Prodehl, C., Gaciri, S., Braile, L.W., Mooney, W.D., Gajewski, D., Sandmeier, K.-J., 1994. Crustal structure beneath the Kenya Rift from axial profile data. Tectonophysics 236, 179–200.

Mechie, J., Keller, G.R., Prodehl, C., Khan, M.A., Gaciri, S.J., 1997. A model for the structure, composition and evolution of the Kenya rift. Tectonophysics 278, 95–119.

Melnick, D., Garcin, Y., Quinteros, J., Strecker, M.R., Olago, D., Tiercelin, J.-J., 2012. Steady rifting in northern Kenya inferred from deformed Holocene lake shorelines of the Suguta and Turkana basins. Earth Planet. Sci. Lett. 331, 335–346.

Mohr, P., Zanettin, B., 1988. The Ethiopian flood basalt province, in: MacDougall, J.D. (Ed.), Continental Flood Basalts. Kluwer Academic, Dordrecht, pp. 63–110.

Mohr, P.A., 1967. Major volcano-tectonic lineament in the Ethiopian rift system. Nature 213, 664–665.

Mohr, P.A., Wood, C.A., 1976. Volcano Spacings and Lithospheric Attenuation in Eastern Rift of Africa. Earth Planet. Sci. Lett. 33, 126–144.

Molin, P., Corti, G., 2015. Topography, river network and recent fault activity at the margins of the Central Main Ethiopian Rift (East Africa). Tectonophysics 664, 67–82.

Mordensky, S.P., Wallace, P.J., 2018. Magma storage below Cascades shield volcanoes as inferred from melt inclusion data: A comparison of long-lived and short-lived magma plumbing systems. J. Volcanol. Geotherm. Res. 368, 1–12.

Morley, C.K., Karanja, F.M., Wescott, W.A., Stone, D.M., Harper, R.M., Wigger, S.T., Day, R.A., 1999. AAPG Studies in Geology# 44, Chapter 2: Geology and Geophysics of the Western Turkana Basins, Kenya.

Morley, C.K., Ngenoh, D.K., 1999. AAPG Studies in Geology# 44, Chapter 1: Introduction to the East African Rift System.

Morrissey, A., Scholz, C.A., 2014. Paleohydrology of Lake Turkana and its influence on the Nile River system. Palaeogeogr. Palaeoclimatol. Palaeoecol. 403, 88–100.

Muirhead, J.D., Kattenhorn, S.A., Lee, H., Mana, S., Turrin, B.D., Fischer, T.P., Kianji, G., Dindi, E., Stamps, D.S., 2016. Evolution of upper crustal faulting assisted by magmatic volatile release during early-stage continental rift development in the East African Rift. Geosphere 12, 1670–1700.

Naliboff, J.B., Buiter, S.J., Péron-Pinvidic, G., Osmundsen, P.T., Tetreault, J., 2017. Complex fault interaction controls continental rifting. Nat. Commun. 8, 1–9.

Newman, S., Lowenstern, J.B., 2002. VolatileCalc: a silicate melt–H2O–CO2 solution model written in Visual Basic for excel. Comput. Geosci. 28, 597–604.

Nutz, A., Schuster, M., Barboni, D., Gassier, G., Van Bocxlaer, B., Robin, C., Ragon, T., Ghienne, J.-F., Rubino, J.-L., 2020. Plio-Pleistocene sedimentation in West Turkana (Turkana Depression, Kenya, East African Rift System): paleolake fluctuations, paleolandscapes and controlling factors. Earth-Sci. Rev. 211, 103415.

Ochieng, J.O., Wilkinson, A.F., Kenya. Ministry of Environment, Natural Resources, 1988. Geology of the Loiyangalani Area: Degree. Ministry of Environment and Natural Resources.

Oppenheimer, C., Moretti, R., Kyle, P.R., Eschenbacher, A., Lowenstern, J.B., Hervig, R.L., Dunbar, N.W., 2011. Mantle to surface degassing of alkalic magmas at Erebus volcano, Antarctica. Earth Planet. Sci. Lett. 306, 261–271.

Orlando, A., Abebe, T., Manetti, P., Santo, A.P., Corti, G., 2006. PETROLOGY OF MANTLE XENOLITHS FROM MEGADO AND DILO; KENYA RIFT; SOUTHERN ETHIOPIA. Ofioliti 31, 71–87.

Parsons, T., Thompson, G.A., 1991. The Role of Magma Overpressure in Suppressing Earthquakes and Topography - Worldwide Examples. Science 253, 1399–1402.

Peccerillo, A., Barberio, M.R., Yirgu, G., Ayalew, D., Barbieri, M., Wu, T.W., 2003. Relationships between mafic and peralkaline silicic magmatism in continental rift settings: A petrological, geochemical and isotopic study of the Gedemsa volcano, central Ethiopian rift. J. Petrol. 44, 2003–2032.

Peron-Pinvidic, G., Manatschal, G., Alves, T., Andersen, T., Andres-Martinez, M., Autin, J., Ball, P., Brune, S., Buiter, S., Cadenas, P., Cresswell, D., Epin, M.E., Gomez-Romeu, J., Gouiza, M., Harkin, C., Heine, C., Hopper, J., Jackson, C., Jolivet, L., Katz, R., Lescoutre, R., Lymer, G., Magee, C., Masini, M., Miro, J., Molnar, N., Mouthereau, F., Muntener, O., Naliboff, J., Norcliffe, J., Osmundsen, P.T., Perez Diaz, L., Phillips, T.P., Ramos, A., Ranero, C., Reston, T., Ribes, C., Rooney, T., Rowan, M., Snidero, M., Tugend, J., Wang, L., Zwaan, F., Partici, Imag.R.W., 2019. Rifted Margins: State of the Art and Future Challenges. Front. EARTH Sci. 7. https://doi.org/10.3389/feart.2019.00218

Pik, R., Deniel, C., Coulon, C., Yirgu, G., Marty, B., 1999. Isotopic and trace element signatures of Ethiopian flood basalts; evidence for plume-lithosphere interactions. Geochim. Cosmochim. Acta 63, 2263–2279.

Pik, R., Marty, B., Hilton, D.R., 2006. How many mantle plumes in Africa? The geochemical point of view. Chem. Geol. 226, 100–114.

Pilet, S., Baker, M.B., Stolper, E.M., 2008. Metasomatized Lithosphere and the Origin of Alkaline Lavas. Science 320, 916–919. https://doi.org/10.1126/science.1156563

Pizzi, A., Coltorti, M., Abebe, B., Disperati, L., Sacchi, G., Salvanini, R., 2006. The Wonjii fault belt (Main Ethiopian Rift): Structural and geomorphological constraints and GPS monitoring., in: Yirgu, G., Ebinger, C., Maguire, P.K.H. (Eds.), The Afar Volcanic Province within the East African Rift System. The Geological Society, London, pp. 191–208.

Prodehl, C., Ritter, J.R.R., Mechie, J., Keller, G.R., Khan, M.A., Jacob, B., Fuchs, K., Nyambok, I.O., Obel, J.D., Riaroh, D., 1997. The KRISP 94 lithospheric investigation of southern Kenya—the experiments and their main results. Tectonophysics 278, 121–147.

Purcell, P.G., 2018. Re-imagining and re-imaging the development of the East African Rift. Pet. Geosci. 24, 21–40.

Rasmussen, D.J., Plank, T.A., Wallace, P.J., Newcombe, M.E., Lowenstern, J.B., 2020. Vapor-bubble growth in olivine-hosted melt inclusions. Am. Mineral. 105, 1898–1919.

Rogers, N., Macdonald, R., Fitton, J.G., George, R., Smith, M., Barreiro, B., 2000. Two mantle plumes beneath the East African Rift system; Sr, Nd and Pb isotope evidence from Kenya Rift basalts. Earth Planet. Sci. Lett. 176, 387–400.

Rogers, N.W., Thomas, L.E., Macdonald, R., Hawkesworth, C.J., Mokadem, F., 2006. U-238-Th-230 disequilibrium in recent basalts and dynamic melting beneath the Kenya rift. Chem. Geol. 234, 148–168. https://doi.org/DOI 10.1016/j.chemgeo.2006.05.002

Rooney, T., Furman, T., Bastow, I.D., Ayalew, D., Gezahegn, Y., 2007. Lithospheric modification during crustal extension in the Main Ethiopian Rift. J. Geophys. Res. B Solid Earth Planets 112, B10201, doi:10.1029/2006JB004916.

Rooney, T., Furman, T., Yirgu, G., Ayalew, D., 2005. Structure of the Ethiopian lithosphere: Xenolith evidence in the Main Ethiopian Rift. Geochim. Cosmochim. Acta 69, 3889–3910.

Rooney, T.O., 2020a. The Cenozoic magmatism of East Africa: Part II–Rifting of the mobile belt. Lithos 360, 105291. https://doi.org/10.1016/j.lithos.2019.105291

Rooney, T.O., 2020b. The Cenozoic magmatism of East Africa: Part III–Rifting of the craton. Lithos 360, 105390. https://doi.org/10.1016/j.lithos.2019.105390

Rooney, T.O., 2020c. The Cenozoic magmatism of East Africa: part V–magma sources and processes in the East African Rift. Lithos 360, 105296. https://doi.org/doi: 10.1016/j.lithos.2019.105296

Rooney, T.O., 2020d. The Cenozoic magmatism of East Africa: Part IV–The terminal stages of rifting preserved in the Northern East African Rift System. Lithos 105381. https://doi.org/10.1016/j.lithos.2019.105381

Rooney, T.O., 2017. The Cenozoic magmatism of East-Africa: Part I—flood basalts and pulsed magmatism. Lithos 286, 264–301.

Rooney, T.O., 2010. Geochemical evidence of lithospheric thinning in the southern Main Ethiopian Rift. Lithos 117, 33–48.

Rooney, T.O., Bastow, I.D., Keir, D., 2011. Insights into extensional processes during magma assisted rifting: Evidence from aligned scoria cones. J. Volcanol. Geotherm. Res. 201, 83–96.

Rooney, T.O., Bastow, I.D., Keir, D., Mazzarini, F., Movsesian, E., Grosfils, E.B., Zimbelman, J.R., Ramsey, M.S., Ayalew, D., Yirgu, G., 2014. The protracted development of focused magmatic intrusion during continental rifting. Tectonics 33, 875–897. https://doi.org/DOI: 10.1002/2013TC003514

Rooney, T.O., Hanan, B.B., Graham, D.W., Furman, T., Blichert-Toft, J., Schilling, J.-G., 2012a. Upper Mantle Pollution during Afar Plume–Continental Rift Interaction. J. Petrol. 53, 365–389. https://doi.org/10.1093/petrology/egr065

Rooney, T.O., Hart, W.K., Hall, C.M., Ayalew, D., Ghiorso, M.S., Hidalgo, P., Yirgu, G., 2012b. Peralkaline magma evolution and the tephra record in the Ethiopian Rift. Contrib. Mineral. Petrol. 164, 407–426.

Rooney, T.O., Krans, S.R., Mège, D., Arnaud, N., Korme, T., Kappelman, J., Yirgu, G., 2018. Constraining the Magmatic Plumbing System in a Zoned Continental Flood Basalt Province. Geochem. Geophys. Geosystems 19, 3917–3944.

Rooney, T.O., Morell, K.D., Hidalgo, P., Fraceschi, P., 2015. Magmatic consequences of the transition from orthogonal to oblique subduction in Panama. Geochem. Geophys. Geosystems 16, 4178–4208. https://doi.org/10.1002/2015gc006150

Rooney, T.O., Nelson, W.R., Ayalew, D., Hanan, B., Yirgu, G., Kappelman, J., 2017. Melting the lithosphere: Metasomes as a source for mantle-derived magmas. Earth Planet. Sci. Lett. 461, 105–118. http://dx.doi.org/10.1016/j.epsl.2016.12.010

Rubin, A.M., 1990. A Comparison of Rift-Zone Tectonics in Iceland and Hawaii. Bull. Volcanol. 52, 302–319.

Rubin, A.M., Pollard, D.D., 1988. Dike-Induced Faulting in Rift Zones of Iceland and Afar. Geology 16, 413–417.

Saria, E., Calais, E., Altamimi, Z., Willis, P., Farah, H., 2013. A new velocity field for Africa from combined GPS and DORIS space geodetic Solutions: Contribution to the definition of the African reference frame (AFREF). J. Geophys. Res. Solid Earth 118, 1677–1697.

Scarsi, P., Craig, H., 1996. Helium isotope ratios in Ethiopian Rift basalts. Earth Planet. Sci. Lett. 144, 505–516.

Shinjo, R., Chekol, T., Meshesha, D., Itaya, T., Tatsumi, Y., 2011. Geochemistry and geochronology of the mafic lavas from the southeastern Ethiopian rift (the East African Rift System): assessment of models on magma sources, plume–lithosphere interaction and plume evolution. Contrib. Mineral. Petrol. 162, 209–230.

Sobolev, A.V., Hofmann, A.W., Kuzmin, D.V., Yaxley, G.M., Arndt, N.T., Chung, S.L., Danyushevsky, L.V., Elliott, T., Frey, F.A., Garcia, M.O., Gurenko, A.A., Kamenetsky, V.S., Kerr, A.C., Krivolutskaya, N.A., Matvienkov, V.V., Nikogosian, I.K., Rocholl, A., Sigurdsson, I.A., Sushchevskaya, N.M., Teklay, M., 2007. The amount of recycled crust in sources of mantle-derived melts. Science 316, 412–417.

Stamps, D.S., Calais, E., Saria, E., Hartnady, C., Nocquet, J.-M., Ebinger, C.J., Fernandes, R.M., 2008. A kinematic model for the East African Rift. Geophys. Res. Lett. 35, L05304. https://doi.org/10.1029/2007GL032781

Stamps, D.S., Saria, E., Kreemer, C., 2018. A geodetic strain rate model for the East African Rift System. Sci. Rep. 8, 1–8.

Steiner, R.A., Rooney, T.O., Girard, G., Rogers, N.W., Ebinger, C., Peterson, L., Phillips, R., 2021. Cenozoic Magmatic Activity in East Africa: New Geochemical Constraints on Magma Distribution within the Eocene Continental Flood Basalt Province, in: Large Igneous Provinces and Their Plumbing Systems. Journal of the Geological Society Special Publications 518.

Sun, S. s-, McDonough, W.F., 1989. Chemical and isotopic systematics of oceanic basalts: Implications for mantle composition and processes., in: Saunders, A.D. (Ed.), Magmatism in the Ocean Basins. Geological Society of London Special Publication 42, pp. 313–345.

Tatsumi, Y., Kimura, N., 1991. Secular variation of basalt chemistry in the Kenya Rift: evidence for the pulsing of asthenospheric upwelling. Earth Planet. Sci. Lett. 104, 99–113.

Tesfaye, S., Harding, D.J., Kusky, T.M., 2003. Early continental breakup boundary and migration of the Afar triple junction, Ethiopia. Geol. Soc. Am. Bull. 115, 1053–1067.

Toplis, M.J., 2005. The thermodynamics of iron and magnesium partitioning between olivine and liquid: criteria for assessing and predicting equilibrium in natural and experimental systems. Contrib. Mineral. Petrol. 149, 22–39.

Trua, T., Deniel, C., Mazzuoli, R., 1999. Crustal control in the genesis of Plio-Quaternary bimodal magmatism of the Main Ethiopian Rift (MER); geochemical and isotopic (Sr, Nd, Pb) evidence. Chem. Geol. 155, 201–231.

Vétel, W., Le Gall, B., Walsh, J.J., 2005. Geometry and growth of an inner rift fault pattern: the Kino Sogo Fault Belt, Turkana Rift (North Kenya). J. Struct. Geol. 27, 2204–2222.

von Höhnel, L.R., 1894. Discovery of Lakes Rudolf and Stefanie: A Narrative of Count Samuel Teleki's Exploring & Hunting Expedition in Eastern Equatorial Africa in 1887 & 1888. Longmans, Green.

Wang, L., Maestrelli, D., Corti, G., Zou, Y., Shen, C., 2021. Normal fault reactivation during multiphase extension: Analogue models and application to the Turkana depression, East Africa. Tectonophysics 811, 228870.

Weinstein, A., Oliva, S.J., Ebinger, C.J., Roecker, S., Tiberi, C., Aman, M., Lambert, C., Witkin, E., Albaric, J., Gautier, S., 2017. Fault-magma interactions during early continental rifting: Seismicity of the M agadi-N atron-M anyara basins, A frica. Geochem. Geophys. Geosystems 18, 3662–3686.

Wiart, P., Oppenheimer, C., 2005. Large magnitude silicic volcanism in north Afar: the Nabro Volcanic Range and Ma'alalta volcano. Bull. Volcanol. 67, 99–115.

WoldeGabriel, G., Aronson, J.L., Walter, R.C., 1990. Geology, geochronology, and rift basin development in the central sector of the Main Ethiopia Rift. Geol. Soc. Am. Bull. 102, 439–458.

Wolfenden, E., Ebinger, C., Yirgu, G., Deino, A., Ayalew, D., 2004. Evolution of the northern Main Ethiopian rift: birth of a triple junction. Earth Planet. Sci. Lett. 224, 213–228.

Wright, T.J., Ebinger, C., Biggs, J., Ayele, A., Yirgu, G., Keir, D., Stork, A., 2006. Magma-maintained rift segmentation at continental rupture in the 2005 Afar dyking episode. Nature 442, 291–294.

Figure 1

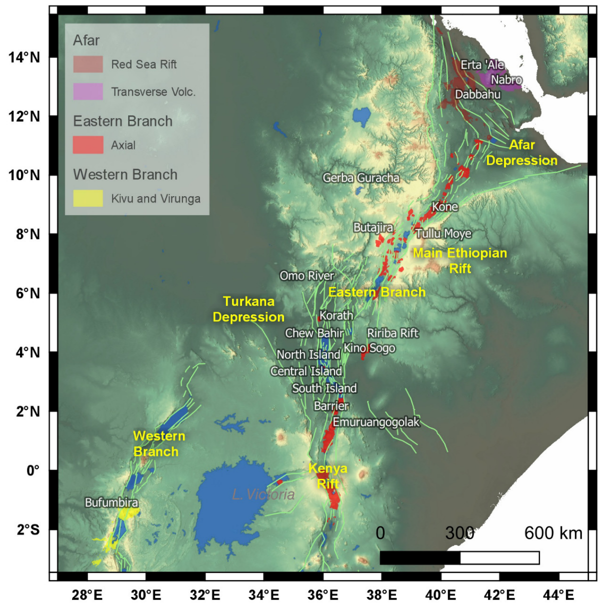
Afar
Red Sea Rift
Transverse Volc.
Eastern Branch
Axial
Western Branch
Kivu and Virunga
Erta 'Ale
Nabro
Dabbahu
Afar Depression
Gerba Guracha
Kone
Butajira
Tullu Moye
Main Ethiopian Rift
Omo River
Eastern Branch
Turkana Depression
Korath
Chew Bahir
Ririba Rift
North Island
Kino Sogo
Central Island
South Island
Barrier
Emuruangogolak
Western Branch
Kenya Rift
L. Victoria
Bufumbira
0
300
600 km
14°N
12°N
10°N
8°N
6°N
4°N
2°N
0°
2°S
28°E
30°E
32°E
34°E
36°E
38°E
40°E
42°E
44°E

Figure 2

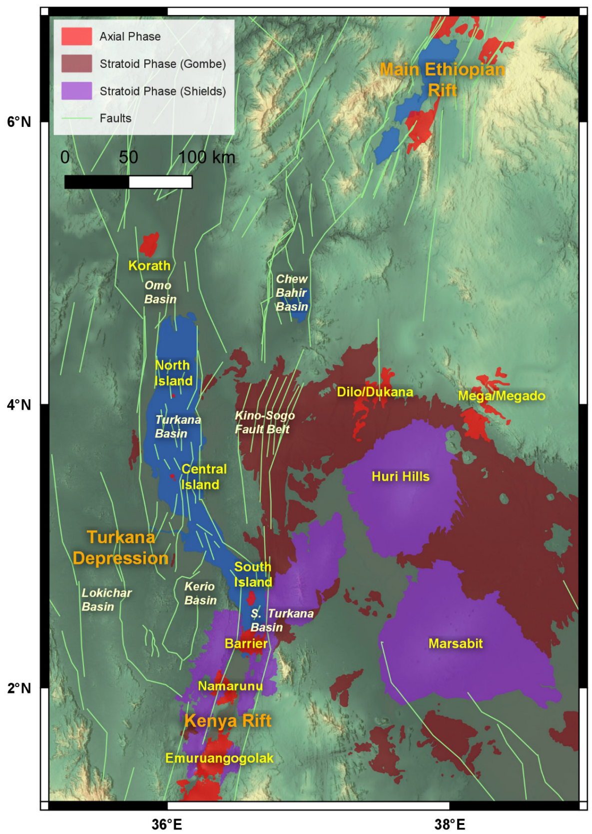
Axial Phase
Stratoid Phase (Gombe)
Stratoid Phase (Shields)
Faults
0
50
100 km
6°N
4°N
2°N
36°E
38°E
Main Ethiopian Rift
Korath
Omo Basin
Chew Bahir Basin
North Island
Dilo/Dukana
Mega/Megado
Turkana Basin
Kino-Sogo Fault Belt
Central Island
Huri Hills
Turkana Depression
South Island
Lokichar Basin
Kerio Basin
S. Turkana Basin
Barrier
Marsabit
Namarunu
Kenya Rift
Emuruangogolak

Figure 3

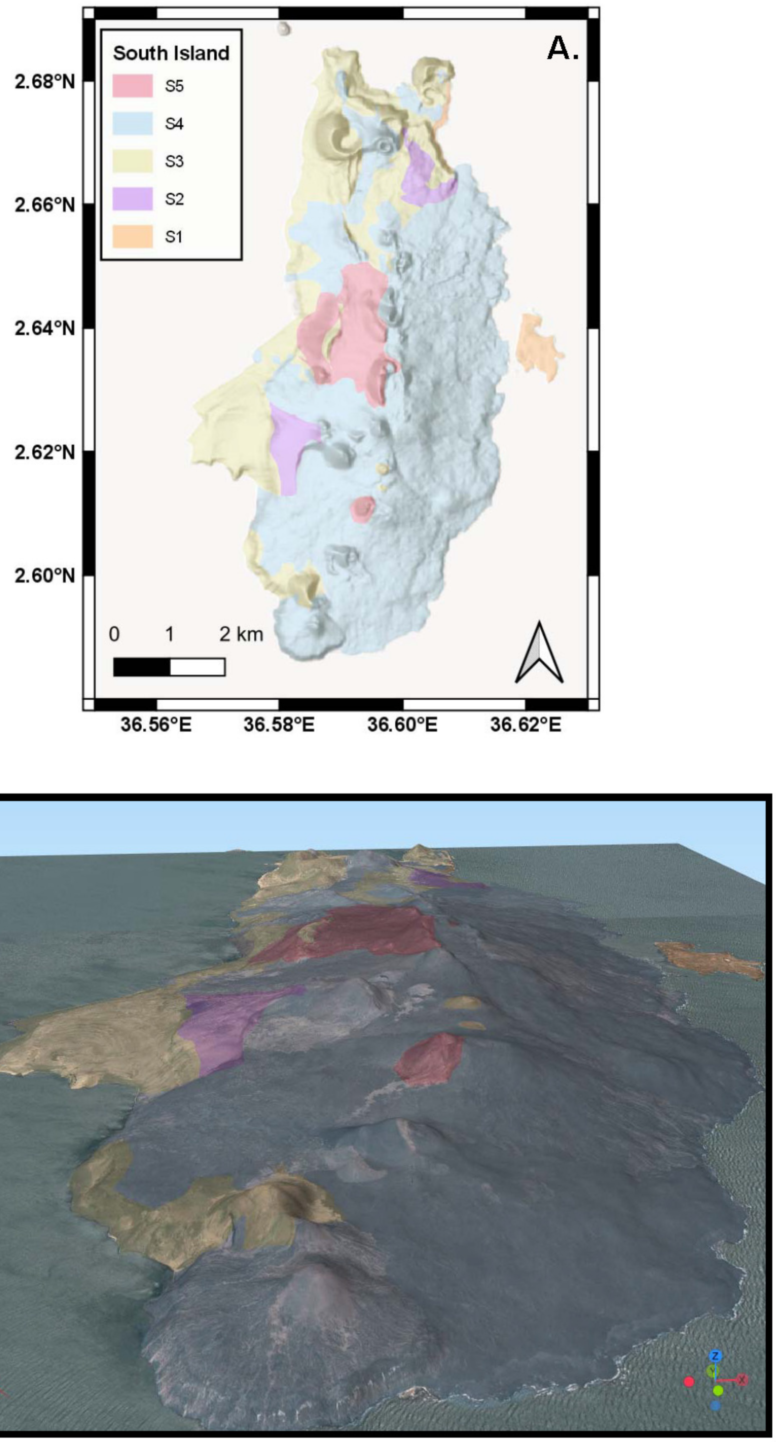
A.
South Island
S5
S4
S3
S2
S1
2.68°N
2.66°N
2.64°N
2.62°N
2.60°N
0 1 2 km
36.56°E
36.58°E
36.60°E
36.62°E
B.

Figure 4

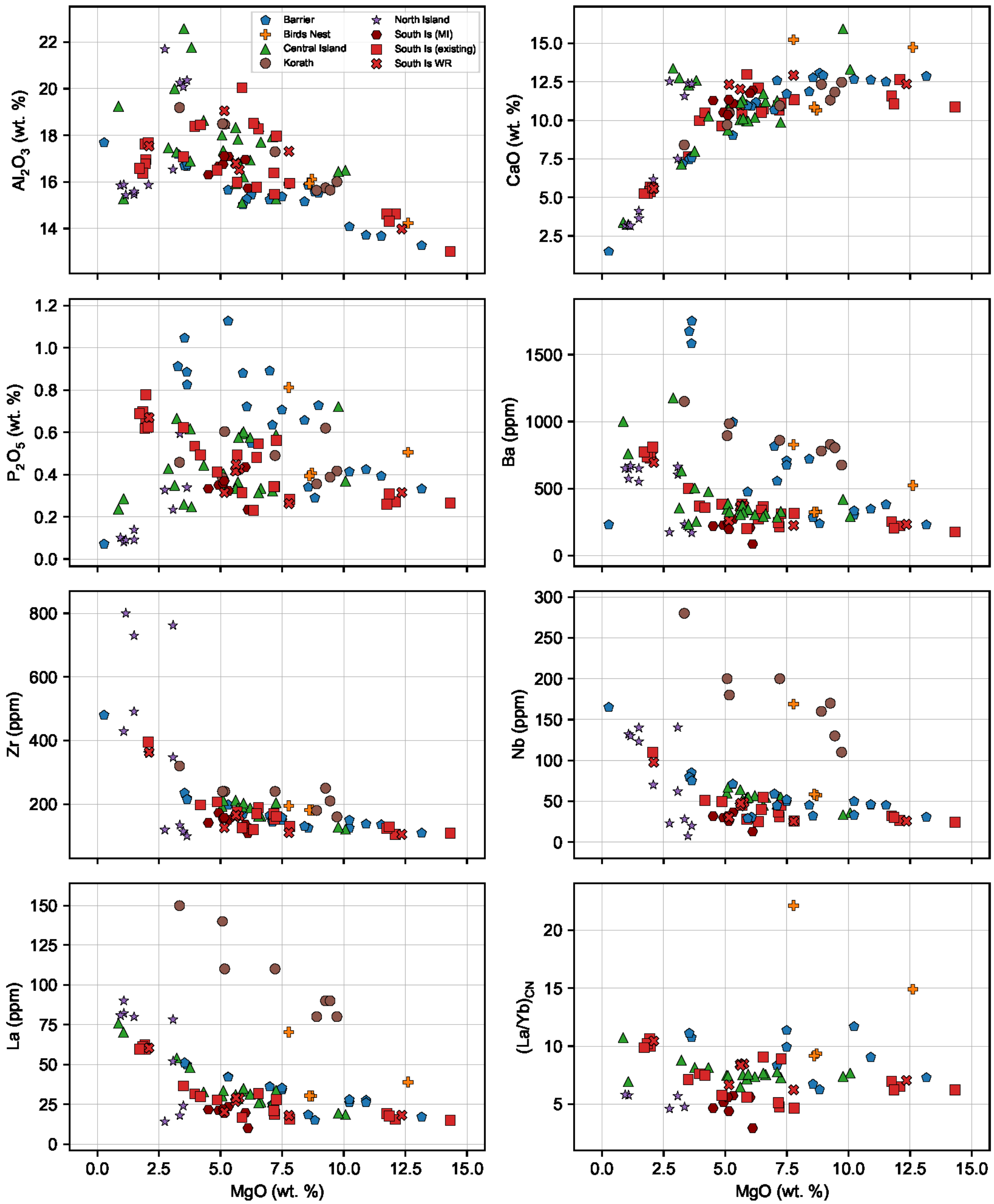

Barrier
Birds Nest
Central Island
Korath
North Island
South Is (MI)
South Is (existing)
South Is WR
Al2O3 (wt. %)
CaO (wt. %)
P2O5 (wt. %)
Ba (ppm)
Zr (ppm)
Nb (ppm)
La (ppm)
(La/Yb)CN
MgO (wt. %)
MgO (wt. %)

Figure 5

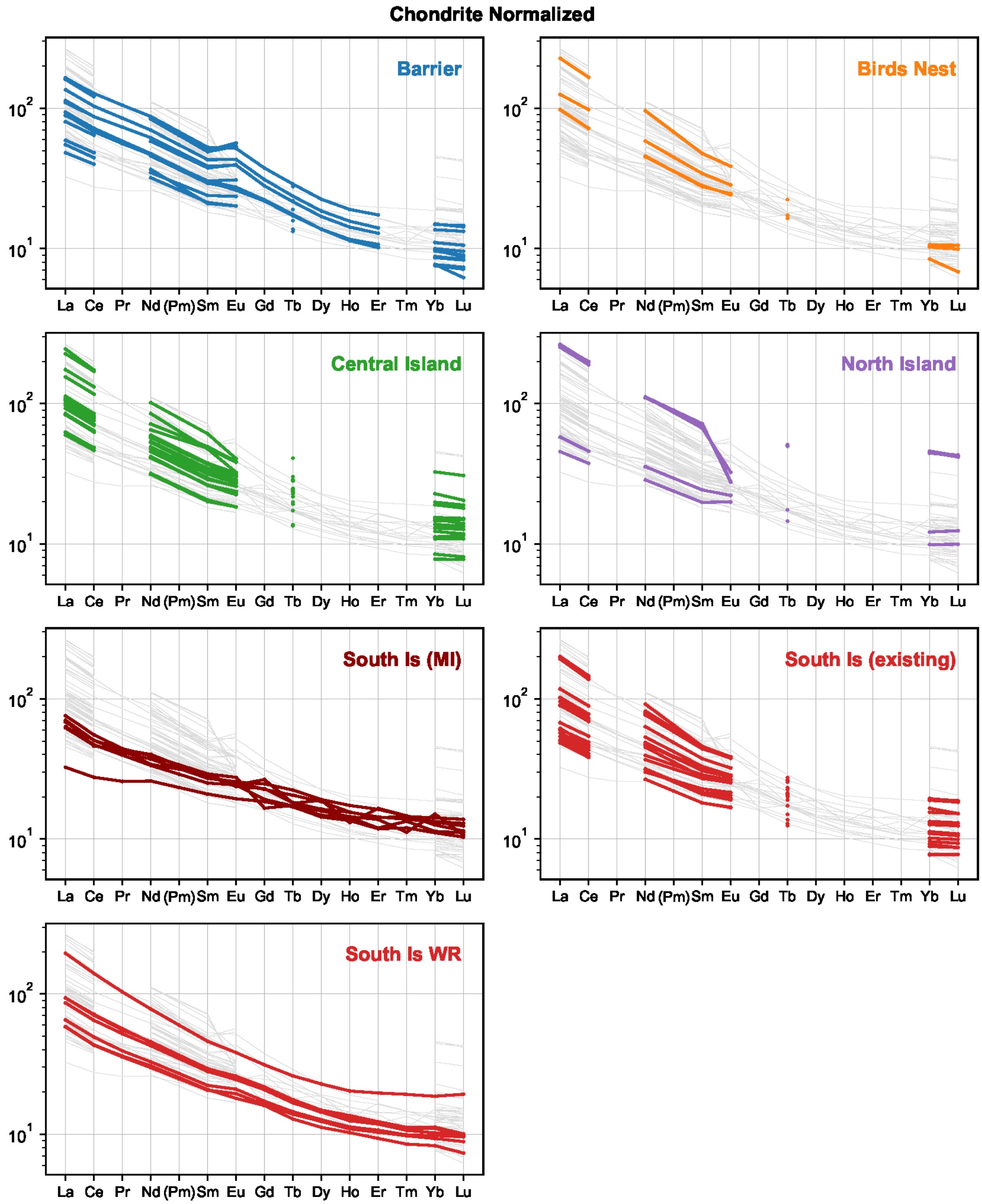

Chondrite Normalized
Barrier
Birds Nest
Central Island
North Island
South Is (MI)
South Is (existing)
South Is WR
$10^2$
$10^1$
La Ce Pr Nd (Pm) Sm Eu Gd Tb Dy Ho Er Tm Yb Lu

Figure 6

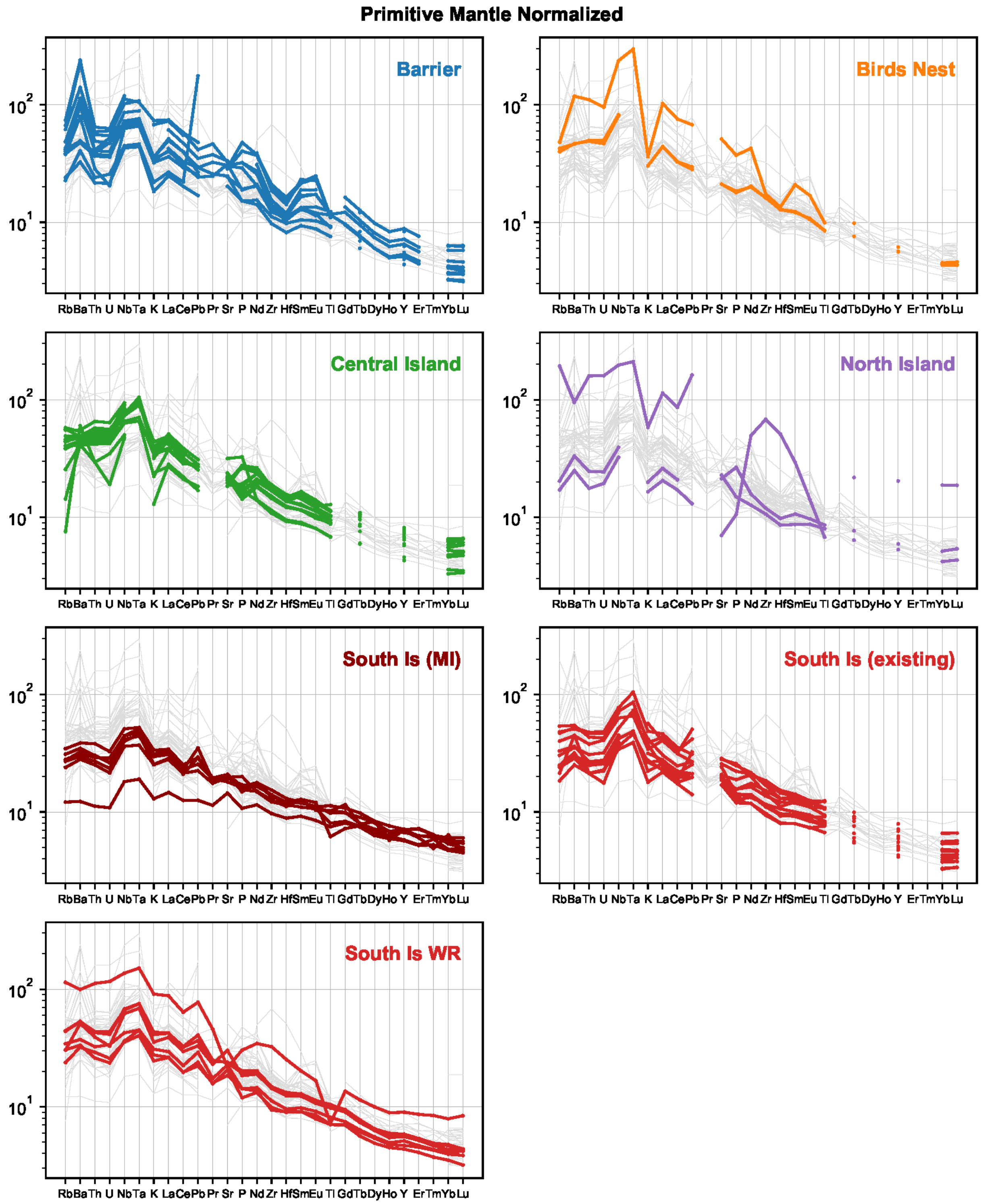
Primitive Mantle Normalized
Barrier
Birds Nest
Central Island
North Island
South Is (MI)
South Is (existing)
South Is WR
10^2
10^1
Rb Ba Th U Nb Ta K La Ce Pb Pr Sr P Nd Zr Hf Sm Eu Ti Gd Tb Dy Ho Y Er Tm Yb Lu

Figure 7

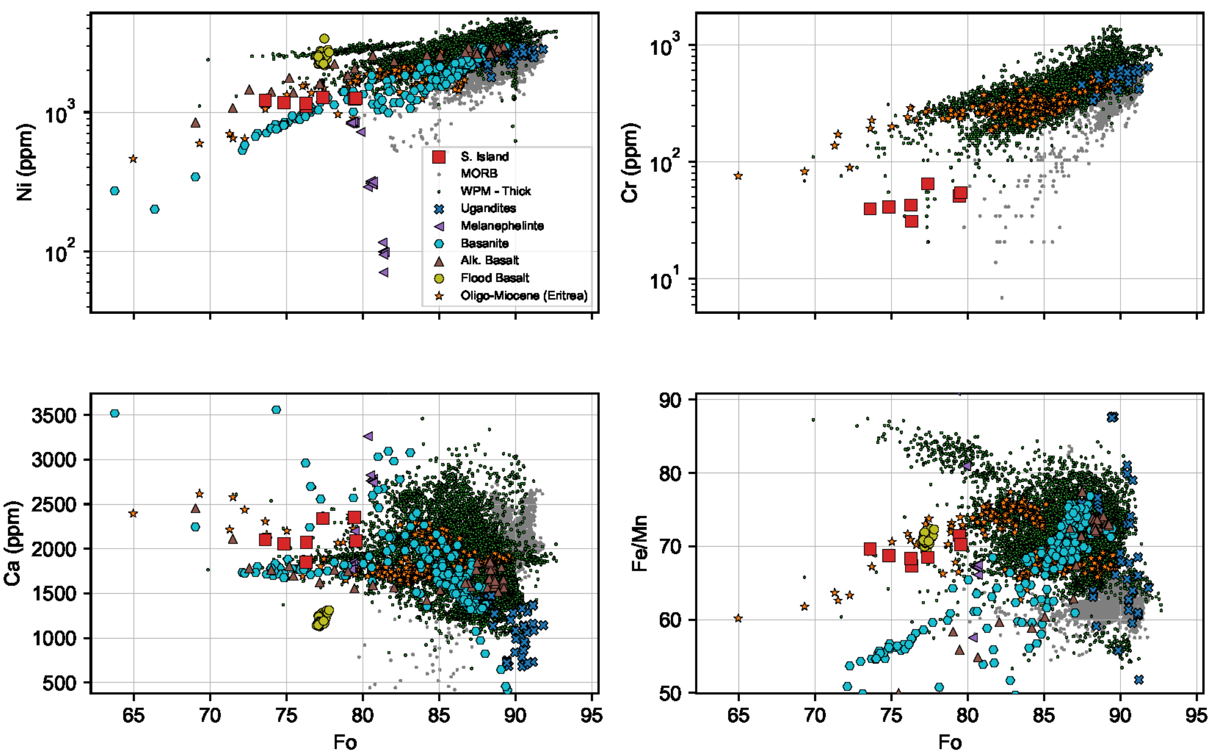

Ni (ppm)
Cr (ppm)
Ca (ppm)
Fe/Mn
Fo
Fo
S. Island
MORB
WPM - Thick
Ugandites
Melanephelinte
Basanite
Alk. Basalt
Flood Basalt
Oligo-Miocene (Eritrea)

Figure 8

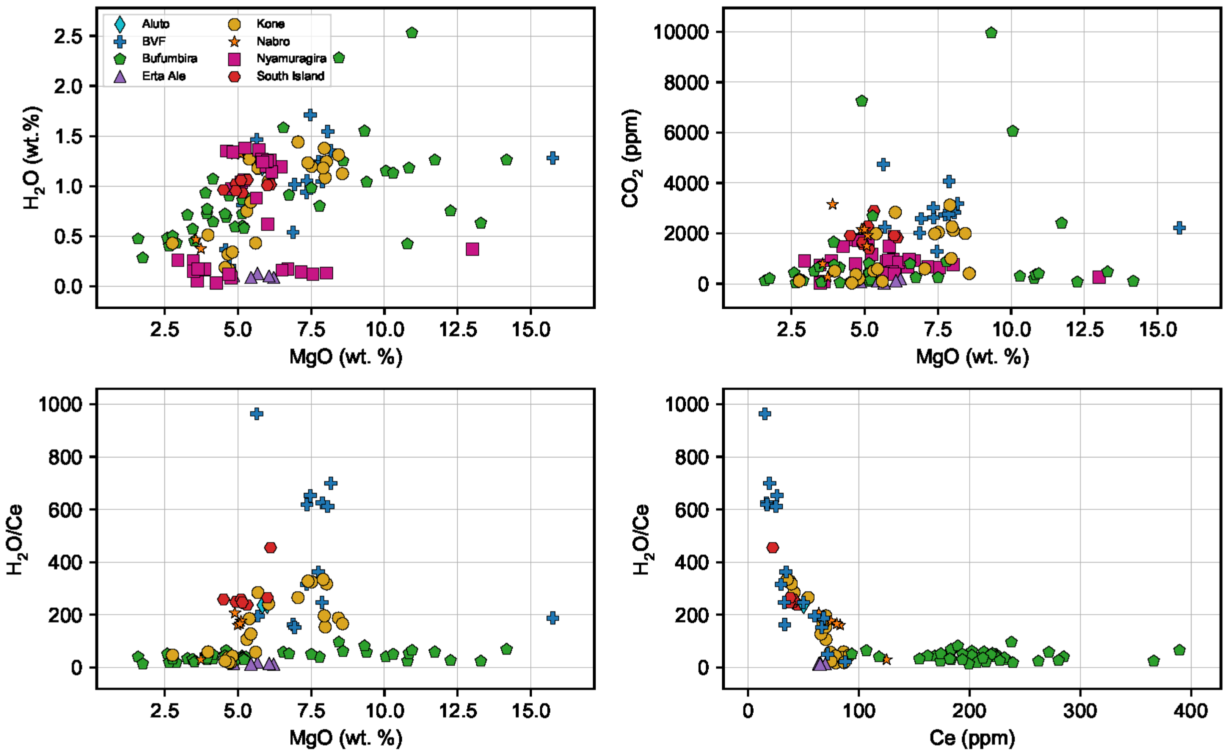

Aluto
BVF
Bufumbira
Erta Ale
Kone
Nabro
Nyamuragira
South Island
$H_2O$ (wt. %)
$CO_2$ (ppm)
$H_2O$/Ce
MgO (wt. %)
Ce (ppm)

1168 Figure 9

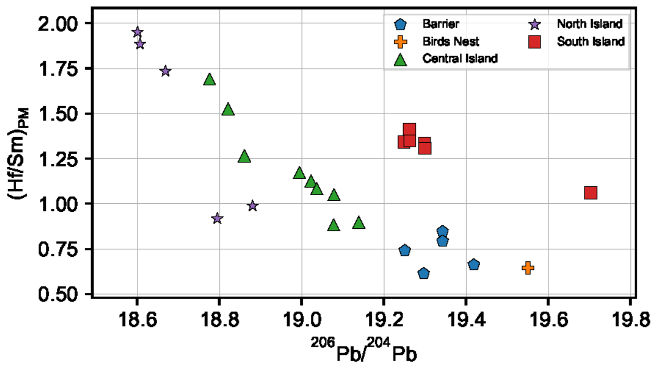


1169

1170 Figure 10

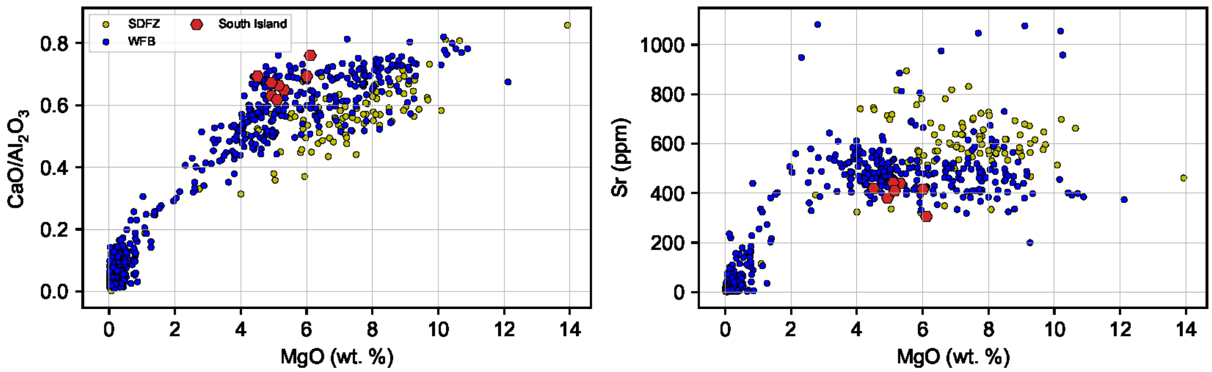


1171

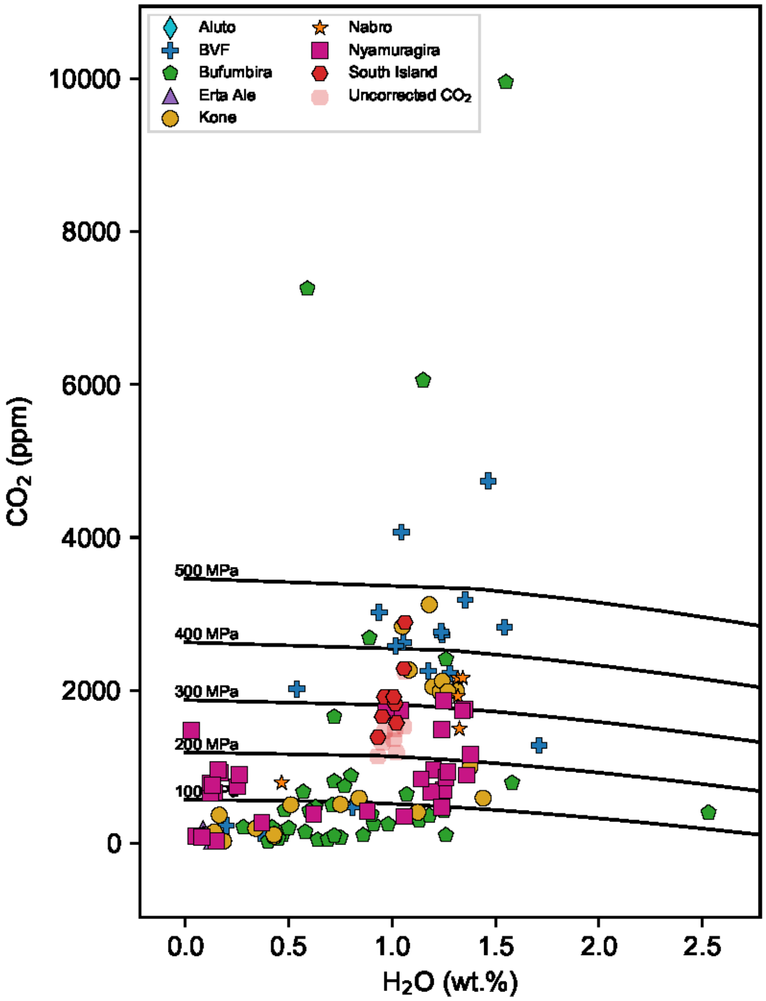
Aluto
BVF
Bufumbira
Erta Ale
Kone
Nabro
Nyamuragira
South Island
Uncorrected $CO_2$
10000
8000
6000
4000
2000
0
$CO_2$ (ppm)
500 MPa
400 MPa
300 MPa
200 MPa
0.0
0.5
1.0
1.5
2.0
2.5
$H_2O$ (wt.%)

Figure 11